Univerzita Karlova v Praze
Matematicko-fyzikální fakulta

DIPLOMOVÁ PRÁCE

Tadeáš Dohnal

Metody určení hierarchie hmot neutrin

Ústav částicové a jaderné fyziky

Vedoucí diplomové práce:	prof. RNDr. Rupert Leitner, DrSc.
Studijní program:	Fyzika
Studijní obor:	Jaderná a subjaderná fyzika

Praha 2016

Charles University in Prague

Faculty of Mathematics and Physics

MASTER THESIS

Tadeáš Dohnal

Methods of determination of neutrino mass hierarchy

Institute of Particle and Nuclear Physics

Supervisor of the master thesis:	prof. RNDr. Rupert Leitner, DrSc.
Study programme:	Physics
Study branch:	Nuclear and Particle Physics

Prague 2016

I declare that I carried out this master thesis independently, and only with the cited sources, literature and other professional sources.

I understand that my work relates to the rights and obligations under the Act No. 121/2000 Sb., the Copyright Act, as amended, in particular the fact that the Charles University in Prague has the right to conclude a license agreement on the use of this work as a school work pursuant to Section 60 subsection 1 of the Copyright Act.

In Prague 14.7.2016

Title: Methods of determination of neutrino mass hierarchy

Author: Tadeáš Dohnal

Institute: Institute of Particle and Nuclear Physics

Supervisor: prof. RNDr. Rupert Leitner, DrSc., Institute of Particle and Nuclear Physics

Abstract: In this thesis, the question of neutrino mass hierarchy is investigated. For this purpose, possibilities of neutrino mass origin are mentioned and phenomenology of neutrino oscillations within three active neutrino framework is introduced. Using that, it is described what neutrino mass hierarchy is and why it would be good to know it. After that, an overview of approaches to this problem is provided, including outline of the JUNO experiment. The approach based on comparison of mass splitting measured in experiments with reactor antineutrinos and accelerator neutrinos is investigated in great detail. The final part of this thesis is measurement of resistive plate chamber properties, as this type of detector was considered to be used in the JUNO experiment (but eventually other type will be used instead).

Keywords: neutrino, neutrino oscillations

I would like to thank my supervisor, prof. RNDr. Rupert Leitner, DrSc., for guidance throughout the process of writing this thesis, Mgr. Viktor Pěč for collaboration on RPC measurement, my family for overall support and Piraňka for making me smile when the work on the thesis didn't go as well as I would have liked.

Contents

Introduction

Neutrinos are electrically neutral leptons. Three generations of leptons have been discovered, each of them containing a charged lepton and a corresponding neutrino: the electron (e^-) and the electron neutrino (ν_e) in the first generation, the muon (μ^-) and the muon neutrino (ν_μ) in the second one, the tauon (τ^-) and the tauon neutrino (ν_τ) in the third one. There is a corresponding antiparticle for each of those particles (e^+, $\overline{\nu}_e$, μ^+, $\overline{\nu}_\mu$, τ^+, $\overline{\nu}_\tau$). However, the question whether neutrino is its own antiparticle or not is still open.

One of the big questions of physics nowadays is the question of neutrino masses. In the simplest version of Standard model, neutrinos were massless, but neutrino oscillations revealed that they have non-zero masses, even though as we know from beta decay, $\overline{\nu}_e$ mass is at least $200\,000\times$ smaller than electron mass. Neutrino oscillations also revealed that neutrino flavour eigenstates are not identical to mass eigenstates as the neutrino flavour can change during its propagation in space-time.

In the first part of this thesis, Dirac and Majorana nature of neutrinos will be described. Then the neutrino mixing and the formalism of neutrino oscillations will be introduced. We shall work in the three active neutrino framework using the PMNS mixing matrix in order to derive transition probabilities for neutrinos propagating in vacuum and matter. Furthermore, current knowledge of oscillation parameters will be summarized, i.e. their values and brief explanations where they came from.

In the second part, the question of the neutrino mass hierarchy will be discussed. We shall look at the reasons for neutrino mass hierarchy determination. Overview of methods capable of resolving this problem will follow. JUNO experiment will be described in a bit more detail. We shall look at its design because resistive plate chambers (RPC) were considered as an option for its muon tracker (eventually other choice was made). Explanation of RPC design and principle of operation will be in the last (fourth) part, followed by description of measurement of Daya Bay type RPC properties and results of the measurement.

In the third part, we shall solely focus on the possibility of resolving mass hierarchy problem by comparing mass splitting measured in electron and muon (anti)neutrino experiments. Several approaches will be discussed.

1. Neutrino Masses and Implications in Physics

1.1 Neutrino Mass Origin

When the Standard Model of particle physics was established, neutrinos were considered to be massless with only left-handed component (right-handed in case of antineutrinos) existent. However, observation of neutrino oscillations provided evidence that neutrino masses are in fact different from zero (or at least most of them as we shall see later). As a consequence, mass term(s) for neutrinos need to be introduced to the Lagrangian, but there are certain differences between neutrinos and the other fermions. First, neutrinos do not have electric charge, and second, while masses of first generation charged fermions are about the order of MeV, all neutrino masses are many orders of magnitude lower than that, not exceeding order of eV. That points to the possibility that neutrino masses may be generated in a different way than those of other fermions.

1.1.1 Dirac mass term

The Dirac mass term represents the most straightforward way of introducing neutrino masses. All other elementary fermions are Dirac particles. The appearance of fermion masses is considered to be a result of breaking of underlying symmetries, but we shall not go to such details here. For one neutrino specie, we can write [1, 2]:

$$\mathcal{L}^D = m_D \bar{\psi} \psi \tag{1.1}$$

where $\mathcal{L}^D$ denotes the part of the Lagrangian responsible for particle mass, $m_D = m_D^*$ mass of the particle and ψ ($\bar{\psi}$) four-component spinor field (Dirac conjugated field). It can be rewritten in the terms of left and right chiral components ψ_L,ψ_R:

$$\mathcal{L}^D = m_D(\bar{\psi}_L \psi_R + \bar{\psi}_R \psi_L) \tag{1.2}$$

In Eq. (1.2) we can see that we need both left-handed and right-handed neutrinos and antineutrinos in order to construct such a mass term. However, right-handed neutrinos (left-handed antineutrinos) do not interact weakly and therefore cannot be directly observed. For this reason, they are usually labelled as sterile neutrinos.

Let's now consider three neutrino flavours ν_l ($l = e, \mu, \tau$). In such case we can write general Dirac mass term in a form [1]

$$\mathcal{L}^D = \sum_{l',l} \bar{\nu}_{l'L} M^D_{l'l} \nu_{lR} + \text{h.c.} \tag{1.3}$$

where $l, l' = e, \mu, \tau$ and M^D is a 3×3 complex matrix. The matrix M^D can be diagonalized by a biunitary transformation [1]:

$$M^D = U^\dagger m^D V \tag{1.4}$$

where U and V are unitary matrices and m^D is a diagonal matrix ($m^D_{ik} = m^D_i \delta_{ik}$). Using U and V, we can rewrite flavour eigenstates ν_l in terms of mass eigenstates

ν_i $(i = 1, 2, 3)$:

$$\nu_{lL} = \sum_{i=1}^{3} U_{li}\nu_{iL} \tag{1.5}$$

$$\nu_{lR} = \sum_{i=1}^{3} V_{li}\nu_{iR} \tag{1.6}$$

Here, the unitary matrix U is the neutrino mixing matrix or Pontecorvo-Maki-Nakagawa-Sakata matrix (PMNS matrix). Using neutrino mass eigenstates ν_i, the Dirac mass term takes form:

$$\mathcal{L}^D = \sum_{i=1}^{3} m_i^D \bar{\nu}_i \nu_i \tag{1.7}$$

In the case of Dirac neutrinos, neutrino and antineutrino are different particles and the total lepton number is in presently known processes conserved.

1.1.2 Majorana mass term

Neutrinos are unique fermions in a way that they do not carry electric charge. That allows a different construction of mass term in addition to the Dirac one. In particular, using the charge-conjugated field ψ^c one can disentangle active (ψ_L) and sterile (ψ_R) neutrino fields by introducing different mass for each kind [2]

$$\mathcal{L}^L = m_L(\bar{\psi}_L(\psi_L)^c + (\bar{\psi_L})^c\psi_L) \tag{1.8}$$

$$\mathcal{L}^R = m_R(\bar{\psi}_R(\psi_R)^c + (\bar{\psi_R})^c\psi_R) \tag{1.9}$$

It is obvious that in a theory of purely Majorana neutrinos the existence of sterile neutrinos is no longer required in order to provide neutrino masses. Expressions (1.8) and (1.9) can be rewritten in the terms of fields ϕ_L and ϕ_R:

$$\phi_L = \psi_L + (\psi_L)^c \qquad \phi_R = \psi_R + (\psi_R)^c \tag{1.10}$$

with the result:

$$\mathcal{L}^L = \frac{1}{2} m_L \bar{\phi}_L \phi_L \tag{1.11}$$

$$\mathcal{L}^R = \frac{1}{2} m_R \bar{\phi}_R \phi_R \tag{1.12}$$

As we can see in Eqs. (1.11),(1.12), the Majorana fields ϕ_L and ϕ_R are mass eigenstates. They also satisfy following conditions:

$$(\phi_L)^c = \phi_L \qquad (\phi_R)^c = \phi_R \tag{1.13}$$

with the meaning that neutrino and antineutrino are in fact the same particle differing only in helicity. It is obvious that the total lepton number is not conserved in such case[1]. Certain processes violating the total lepton number by 2 are possible, most notably neutrinoless double beta decay $(0\nu\beta\beta)$ which is investigated in number of experiments (more in Chapter 2).

---

[1] It also requires non-zero neutrino masses because otherwise the helicity is fixed.

As in the previous case we can generalize equations above to the case of three neutrino flavours ν_l ($l = e, \mu, \tau$). Since active and sterile neutrinos are disentangled, we shall consider only active (ν_{lL}) neutrinos; nevertheless, one can proceed in the same way when considering sterile neutrinos. The mass term for three active neutrinos then takes form [1, 2]

$$\mathcal{L}^L = \frac{1}{2}\sum_{l',l} \bar{\nu}_{l'L} M^L_{l'l} (\nu_{lL})^c + \text{h.c.} \tag{1.14}$$

where $l, l' = e, \mu, \tau$ and M^M is a 3×3 symmetric matrix which can be diagonalized using a unitary matrix U:

$$M^M = U m^L U^T \tag{1.15}$$

In analogy to the Dirac case, m^L is a diagonal matrix ($m^L_{ik} = m^L_i \delta_{ik}$). By defining

$$\nu_{iL} = U^\dagger \nu_L + (U^\dagger \nu_L)^c \tag{1.16}$$

we can rewrite the Majorana mass term of active neutrinos to the form:

$$\mathcal{L}^L = \frac{1}{2}\sum_{i=1}^{3} m^L_i \bar{\nu}_{iL} \nu_{iL} \tag{1.17}$$

Thus ν_{Li} are mass eigenstates which satisfy Majorana condition:

$$(\nu_{iL})^c = \nu_{iL} \tag{1.18}$$

1.1.3 Dirac and Majorana mass term

In the most general case we can put both Dirac and Majorana mass terms to the Lagrangian. That naturally requires both active and sterile neutrinos to be considered:

$$\mathcal{L}^{DM} = m_D \bar{\psi}_L \psi_R + \frac{1}{2} m_L \bar{\psi}_L (\psi_L)^c + \frac{1}{2} m_R \bar{\psi}_R (\psi_R)^c + \text{h.c.} \tag{1.19}$$

This can be further altered [2]:

$$\mathcal{L}^{DM} = \frac{1}{2}\left[m_D(\bar{\psi}_L \psi_R + (\bar{\psi}_L)^c (\psi_R)^c) + m_L \bar{\psi}_L (\psi_L)^c + m_R \bar{\psi}_R (\psi_R)^c\right] + \text{h.c.} \tag{1.20}$$

Let's define:

$$n = \begin{pmatrix} \psi_L \\ (\psi_R)^c \end{pmatrix} \qquad M^{DM} = \begin{pmatrix} m_L & m_D \\ m_D & m_R \end{pmatrix} \tag{1.21}$$

This allows us to rewrite Eq. (1.20) in a form:

$$\mathcal{L}^{DM} = \frac{1}{2}(\bar{n} M^{DM} n^c + \bar{n}^c M^{DM} n) \tag{1.22}$$

Being a symmetric matrix, M^{DM} can be diagonalized by an orthogonal transformation. Let's consider an orthogonal matrix O:

$$O = \begin{pmatrix} \cos\alpha & \sin\alpha \\ -\sin\alpha & \cos\alpha \end{pmatrix} \tag{1.23}$$

The diagonalization takes form:

$$M^{DM} = Om^{DM}O^T \tag{1.24}$$

where m^{DM} is a diagonal matrix with values on the diagonal [1, 2]:

$$m_{1,2}^{DM} = \frac{1}{2}(m_L + m_R) \mp \frac{1}{2}\sqrt{(m_R - m_L)^2 + 4m_D^2} \tag{1.25}$$

It is obvious that for certain values of m_L, m_R, m_D (for example $m_D \gg m_L$, m_R) m_1^{DM} has a negative value. In such case, the transformation has to be slightly altered. Instead of orthogonal transformation O we use a unitary transformation

$$U = O\begin{pmatrix} i & 0 \\ 0 & 1 \end{pmatrix} \tag{1.26}$$

in order to obtain diagonal matrix $\tilde{m}^{DM}$ with positive values on the diagonal ($|m_{1,2}^{DM}|$):

$$M^{DM} = U\tilde{m}^{DM}U^T \tag{1.27}$$

Then we can define mass eigenstates:

$$n^m = O^\dagger n + (O^\dagger n)^c\,, \text{ respectively } n^m = U^\dagger n + (U^\dagger n)^c \tag{1.28}$$

and using them we can rewrite the mass term to the form:

$$\mathcal{L}^{DM} = \frac{1}{2}\sum_{i=1}^{2} |m_i^{DM}|\bar{n}_i^m n_i^m \tag{1.29}$$

If we take a left-handed projection of equation (1.28), we get relation for the active left-handed flavour neutrino field:

$$\psi_L = n_1^m \cos\alpha + n_2^m \sin\alpha, \text{ respectively } \psi_L = in_1^m \cos\alpha + n_2^m \sin\alpha \tag{1.30}$$

Seesaw mechanism

Perhaps the most renown explanation of smallness of neutrino masses with respect to the masses of other fermions is so called *seesaw mechanism*. The main idea is that the neutrino Dirac mass term (m_D) is of the same order as other fermions' and the actual smallness of neutrino masses results from mixing with Majorana mass terms. To achieve that, let's assume that $m_L = 0$ and $m_R \gg m_D$. Evaluating (1.25) in this particular case, we obtain [1]:

$$m_1^{DM} \simeq \frac{2m_D^2}{m_R} \gg m_D, \quad m_2^{DM} \simeq m_R, \quad \alpha =\simeq \frac{m_D}{m_R} \tag{1.31}$$

From equation (1.30) we can see that due to the smallness of α the active neutrino field ψ_L consist mostly of the lighter mass eigenstate n_1^m.

Generalization for three neutrino flavours

The problem of combined Dirac and Majorana mass term can be generalized for three neutrinos flavours. In such case, ψ_L and ψ_R are vectors of three fields (electron, muon and tauon flavour) and consequently M^{DM} is a 6 × 6 matrix instead of 2 × 2 matrix. It needs to be diagonalized by a unitary transformation U represented by a 6 × 6 matrix. That is much more complicated to write in an explicit form, so we shall not go into detail. It is just worth mentioning that the seesaw mechanism can be generalized to three neutrino flavours as well [1].

1.2 Direct measurement of neutrino masses

Neutrino masses have not been directly determined yet; only upper bounds have been estimated so far. The most stringent one comes from precise measurement of kinematics of β-decay of ^{3}H. The spectrum of electrons around the end point depends on $\overline{\nu}_e$ mass and by measuring it precisely $\overline{\nu}_e$ mass can be determined. However, the mass is below sensitivity of experiments that have been carried out so far. The most precise result comes from Troitsk experiment claiming $m_{\overline{\nu}_e} < 2.05\,\mathrm{eV}$ or $2.12\,\mathrm{eV}$ at 95% CL depending on analysis approach [3]. The Mainz experiment phase II came to result $m_{\overline{\nu}_e} < 2.3\,\mathrm{eV}$ at 95% CL [4].

With first run planned to 2017, the KATRIN experiment is designed to reach sensitivity of $0.2\,\mathrm{eV}$ at 90% CL within approximately five calendar years [5].

If neutrinos are Majorana particles, there are also limits resulting from measurement of neutrinoless double beta decay. The most stringent upper bound for effective ν_e mass, $0.060 - 0.161\,\mathrm{eV}$ at 90% CL (depending on nuclear matrix element), comes from KamLAND-Zen experiment [6], we shall discuss neutrinoless double beta decay in more detail in Chapter 2.

1.3 Neutrino mixing

As we saw in the previous section, neutrino flavour eigenstates are connected to the mass eigenstates by a unitary transformation. Although the nature of neutrino mass origin (i.e. whether neutrinos are Dirac or Majorana particles) is currently unknown, the existence of neutrino mixing that allows neutrino oscillations is an experimental fact. Let's look into it in more detail, conveniently using bra-ket notation:

$$|\nu_\alpha\rangle = \sum_{i=1}^{3} U^*_{\alpha i}\,|\nu_i\rangle \tag{1.32}$$

where $|\nu_\alpha\rangle$ is a neutrino flavour eigenstate, $|\nu_i\rangle$ is a neutrino mass eigenstate (unless stated otherwise, Greek index will denote flavour eigenstate and latin index will denote mass eigenstate) and U is the unitary matrix connecting them, usually called Pontecorvo-Maki-Nakagawa-Sakata (PMNS) matrix. Its elements can be written in a way:

$$U_{\alpha i} \equiv \langle\nu_\alpha|\nu_i\rangle \tag{1.33}$$

By using the CPT symmetry we get analogous expression for antineutrinos:

$$\overline{U}_{\alpha i} \equiv \langle\overline{\nu}_\alpha|\overline{\nu}_i\rangle = \langle\nu_i|\nu_\alpha\rangle \equiv U^*_{\alpha i} \tag{1.34}$$

And in analogy to Eq. (1.32) we get:

$$|\overline{\nu}_\alpha\rangle = \sum_{i=1}^{3} U_{\alpha i}\,|\overline{\nu}_i\rangle \tag{1.35}$$

1.3.1 PMNS matrix

The PMNS matrix is in general $n \times n$ complex unitary matrix. Such a matrix is determined by n^2 independent parameters: $\frac{1}{2}n(n-1)$ angles and $\frac{1}{2}n(n+1)$

phases. Out of that, n phases can be removed by redefining n non-physical phases of charged leptons. If neutrinos are Dirac particles, we can redefine $(n-1)$ more phases in a similar way which leaves the PMNS matrix with $\frac{1}{2}(n-1)(n-2)$ phases and $(n-1)^2$ parameters in total. The later is not possible for Majorana neutrinos because their phases are fixed and therefore the PMNS matrix has $\frac{1}{2}n(n-1)$ phases and $n(n-1)$ parameters in total [7].

There are three currently known (active) neutrino flavours and a strong evidence coming from the decay of Z boson that there are no other (lighter than approx. 45 GeV). While the existence of sterile neutrinos cannot be completely ruled out, most of the neutrino oscillations experiments use the three active neutrino flavours framework (or even a two neutrino flavours approximation) and we shall use that as well. In such case, it is possible to write the PMNS matrix in terms of three mixing angles θ_{12}, θ_{13}, θ_{23}, one CP violating phase δ and two Majorana phases α_1, α_2 (description of the formalism can be found in [1, 2, 7, 8]):

$$U_{\alpha i} = \begin{pmatrix} 1 & 0 & 0 \\ 0 & c_{23} & s_{23} \\ 0 & -s_{23} & c_{23} \end{pmatrix} \begin{pmatrix} c_{13} & 0 & s_{13}e^{-i\delta} \\ 0 & 1 & 0 \\ -s_{13}e^{i\delta} & 0 & c_{13} \end{pmatrix} \cdot$$

$$\cdot \begin{pmatrix} c_{12} & s_{12} & 0 \\ -s_{12} & c_{12} & 0 \\ 0 & 0 & 1 \end{pmatrix} \begin{pmatrix} e^{i\alpha_1/2} & 0 & 0 \\ 0 & e^{i\alpha_2/2} & 0 \\ 0 & 0 & 1 \end{pmatrix} \tag{1.36}$$

where s_{ij} stands for $sin(\theta_{ij})$ and c_{ij} for $cos(\theta_{ij})$. When dealing with neutrino oscillations, the Majorana phases do not affect the transition probabilities and can be neglected. The PMNS matric then takes form:

$$U_{\alpha i} = \begin{pmatrix} c_{12}c_{13} & s_{12}c_{13} & s_{13}e^{-i\delta} \\ -s_{12}c_{23} - c_{12}s_{23}s_{13}e^{i\delta} & +c_{12}c_{23} - s_{12}s_{23}s_{13}e^{i\delta} & s_{23}c_{13} \\ +s_{12}s_{23} - c_{12}c_{23}s_{13}e^{i\delta} & -c_{12}s_{23} - s_{12}c_{23}s_{13}e^{i\delta} & c_{23}c_{13} \end{pmatrix} \tag{1.37}$$

1.4 Neutrino oscillations

The idea of neutrino oscillations dates back to 1957 when it was proposed by Bruno Pontecorvo and in 1962 further elaborated by Z. Maki, M. Nakagawa and S. Sakata. Later the solar neutrinos problem arose when only about one third of the theoretical flux was detected. The idea of oscillations was reviewed as an explanation of the deficit. The first compelling evidence for neutrino oscillations was provided in 1998 by the Super-Kamiokande experiment measuring atmospheric neutrinos. Since then, many experiments investigating neutrino oscillations have been carried out to a great success.

As we shall see, the phenomenon of neutrino oscillations is closely tied to the neutrino masses, in fact it cannot occur if all the neutrino masses are zero.

1.4.1 Neutrino oscillations in vacuum

This section is based on [1, 2, 7, 8].

Assuming that all neutrinos we actually deal with are highly relativistic, we can make following approximation:

$$E_i = \sqrt{p_i^2 + m_i^2} \cong p_i + \frac{m_i^2}{2E_i} \tag{1.38}$$

Now let's assume that a flavoured neutrino $|\nu_\alpha\rangle$ is created along with a corresponding charged lepton. As we see in Eq. (1.32), $|\nu_\alpha\rangle$ can be written as a superposition of mass eigenstates $|\nu_i\rangle$, each having energy E_i and momentum p_i. Propagation of such state to distance L in time t can be then described:

$$|\nu_i(t, L)\rangle = e^{ip_iL}e^{-iE_it}\,|\nu_i\rangle = e^{-i(E_it-p_iL)}\,|\nu_i\rangle \tag{1.39}$$

The evolution of a flavour eigenstate is then:

$$|\nu_\alpha(t, L)\rangle = \sum_{i=1}^{3} U^*_{\alpha i}\,|\nu_i(t, L)\rangle \tag{1.40}$$

Now we can derive the probability $P_{\alpha\beta}$ of finding (measuring) a neutrino in the flavour eigenstate $|\nu_\beta\rangle$ whereas the eigenstate in which the neutrino was created is $|\nu_\alpha\rangle$:

$$P_{\alpha\beta} = |\,\langle\nu_\beta|\nu_\alpha(t, L)\rangle\,|^2 = |\sum_{i=1}^{3}\sum_{j=1}^{3} U^*_{\alpha i}U_{\beta j}\,\langle\nu_j|\nu_i(t, L)\rangle\,|^2 \tag{1.41}$$

Analogous formula can be derived for antineutrinos using Eq. (1.35). Applying neutrino propagation formula (1.39) to Eq. (1.41) we get:

$$P_{\alpha\beta} = \sum_{i=1}^{3}\sum_{j=1}^{3} e^{-i\phi_{ij}(L,t)}U^*_{\alpha i}U_{\beta i}U_{\alpha j}U^*_{\beta j} \tag{1.42}$$

where $\phi_{ij}(t, L)$ is a relative phase factor caused by different propagation of various neutrino mass eigenstates $|\nu_i\rangle$:

$$\phi_{ij}(t, L) = (E_i - E_j)t - (p_i - p_j)L \cong \frac{(m_i^2 - m_j^2)L}{2E} \equiv \frac{\Delta m^2_{ij}L}{2E} \tag{1.43}$$

Further altering Eq. (1.42) we get (restoring $\hbar$ and c):

$$P_{\alpha\beta} = \delta_{\beta\alpha} - 4\sum_{i<j}\mathrm{Re}[U^*_{\alpha i}U_{\beta i}U_{\alpha j}U^*_{\beta j}]\sin^2\left(\frac{\Delta m^2_{ij}L}{4E\hbar c}\right) + \\ + 2\sum_{i<j}\mathrm{Im}[U^*_{\alpha i}U_{\beta i}U_{\alpha j}U^*_{\beta j}]\sin\left(\frac{\Delta m^2_{ij}L}{2E\hbar c}\right) \tag{1.44}$$

The first two terms of Eq. (1.44) are affected neither by interchange of the initial and final neutrino state ($P_{\alpha\beta} = P_{\beta\alpha}$, T-symmetry) nor by interchange of neutrino and antineutrino ($P_{\alpha\beta} = P_{\overline{\alpha\beta}}$, CP-symmetry).

The third term of Eq. (1.44) is nonzero only if CP- and T-symmetries are violated in neutrino oscillations. That would mean that the PMNS matrix is complex due to $\delta \neq 0, \pi$. In such case $P_{\alpha\beta} \neq P_{\beta\alpha}$, $P_{\alpha\beta} \neq P_{\overline{\alpha\beta}}$; nevertheless CPT-symmetry grants $P_{\alpha\beta} = P_{\overline{\beta\alpha}}$.

Let us focus on the CP-symmetry conserving part (the first two terms in Eq. (1.44)). As we can see, the transition probability $P_{\alpha\beta}$ has an oscillatory behaviour with the distance between two maxima (or minima) measured in L/E dependant on the difference of squares of neutrino masses $m_i^2 - m_j^2 = \Delta m^2_{ij}$:

$$\frac{L}{E} = \frac{4\pi\hbar c}{\Delta m^2_{ij}} \tag{1.45}$$

If we evaluate constants in the phase factor ϕ_{ij}, we get:

$$\frac{\phi_{ij}}{2} \equiv \frac{\Delta m_{ij}^2 L}{4E\hbar c} \doteq 1.27 \left(\frac{\Delta m_{ij}^2}{\mathrm{eV}^2}\right) \left(\frac{L}{\mathrm{km}}\right) \left(\frac{\mathrm{GeV}}{E}\right) \tag{1.46}$$

In experiments, a common choice is to place a detector to the first disappearance minimum (appearance maximum) for which the following formula applies (using the same units as in Eq. (1.46)):

$$\frac{L}{E} = \frac{\pi}{2.54 \Delta m_{ij}^2} \tag{1.47}$$

1.4.2 Neutrino oscillations in matter

In general, neutrino time evolution can be described by following equation [1]:

$$i \frac{\partial \left|\nu(t)\right\rangle}{\partial t} = H \left|\nu(t)\right\rangle \tag{1.48}$$

where H is Hamiltonian. So far we have only considered the free particle Hamiltonian. On the contrary, when neutrino passes through matter, interaction Hamiltonian has to be taken into account as well because of coherent scattering.

Coherent scattering of a neutrinos can happen in two ways - via charge current (CC) and neutral current (NC). NC interaction is the same for all neutrino flavours and therefore it only affects the common phase of neutrinos a does not alter neutrino oscillations. The situation is markedly different when one considers CC interaction. Since all common matter contains electrons, but no muons nor tauons, only ν_e, $\overline{\nu}_e$ are affected.

Let's consider a flavour neutrino vector $\nu_\alpha = (\nu_e, \nu_\mu, \nu_\tau)$. We can describe its time evolution (description of neutrino oscillation in matter is in [1, 2, 7, 8]):

$$i \frac{\partial \left|\nu_\alpha(t)\right\rangle}{\partial t} = H^m \left|\nu_\alpha(t)\right\rangle = (UH^0U^\dagger + H^{NC} + H^{CC}) \left|\nu_\alpha(t)\right\rangle \tag{1.49}$$

where U is PMNS mixing matrix, H^0 matrix corresponds to free particle evolution described above, H^{NC} denotes the NC part of the Hamiltonian (proportional to identity matrix and not affecting neutrino oscillations) and H^{CC} is CC interaction Hamiltonian:

$$H_m^0 = \frac{1}{2E} \begin{pmatrix} m_1^2 & 0 & 0 \\ 0 & m_2^2 & 0 \\ 0 & 0 & m_3^2 \end{pmatrix} \qquad H^{CC} = \begin{pmatrix} \sqrt{2} N_e G_F & 0 & 0 \\ 0 & 0 & 0 \\ 0 & 0 & 0 \end{pmatrix} \tag{1.50}$$

where N_e is electron density and G_F is Fermi coupling constant. When dealing with antineutrinos, the only difference is opposite sign in H^{CC} term ($\sqrt{2}N_eG_F \rightarrow -\sqrt{2}N_eG_F$). Only $UH_m^0U^\dagger$ and H^{CC} are relevant for neutrino oscillations.

If $N_e \neq 0$, the Hamiltonian is no longer diagonalized by U. Altered U^m needs to be used instead:

$$H^m = U^m E^m U^{m\dagger} \tag{1.51}$$

where E^m stands for diagonal matrix $Diag(E_1^m, E_2^m, E_3^m)$.

Since for $N_e \neq 0$ we have $U^m \neq U$, neutrino mixing is altered and because the sign in H^{CC} differs for neutrinos and antineutrinos, they are affected differently. Oscillation length depending on E^m is altered as well.

Two-neutrino approximation

It is both illustrative and actually useful to look how the matter affects neutrino oscillation in two-neutrino framework of ν_α, ν_β flavour eigenstates and ν_i, ν_j mass eigenstates with square mass difference Δm^2 and mixing angle θ. Subtracting appropriate multiple of unit matrix that does not affect the oscillations, we get [8]:

$$i\frac{\partial}{\partial t}\begin{pmatrix}\nu_\alpha(t)\\ \nu_\beta(t)\end{pmatrix} = \tilde{H}^m \begin{pmatrix}\nu_\alpha(t)\\ \nu_\beta(t)\end{pmatrix} = \frac{\Delta m^2_{ji}}{4E}\begin{pmatrix}-(\cos 2\theta - V) & \sin 2\theta\\ \sin 2\theta & (\cos 2\theta - V)\end{pmatrix}\begin{pmatrix}\nu_\alpha(t)\\ \nu_\beta(t)\end{pmatrix} \tag{1.52}$$

where

$$V = \frac{2\sqrt{2}}{\Delta m^2}EN_eG_F \tag{1.53}$$

We can rewrite $\tilde{H}^m$:

$$\tilde{H}^m = \frac{\Delta m^2_m}{4E}\begin{pmatrix}-\cos 2\theta^m & \sin 2\theta^m\\ \sin 2\theta^m & \cos 2\theta^m\end{pmatrix} \tag{1.54}$$

where

$$\sin 2\theta^m = \frac{\sin 2\theta}{\sqrt{(\cos 2\theta - V)^2 + \sin^2 2\theta}} \tag{1.55}$$

$$\cos 2\theta^m = \frac{\cos 2\theta - V}{\sqrt{(\cos 2\theta - V)^2 + \sin^2 2\theta}} \tag{1.56}$$

$$\Delta m^2_m = \Delta m^2_{ji}\sqrt{(\cos 2\theta - V)^2 + \sin^2 2\theta} \tag{1.57}$$

It is obvious that for $N_e = 0$ ($\to V = 0$) we obtain neutrino oscillations in vacuum. The same approximately holds for $|V| \ll \cos 2\theta$. On the contrary, for $V = \cos 2\theta$ we get $\sin 2\theta^m = 1$ and mixing becomes maximal. For $|V| \gg \cos 2\theta$, $\sin 2\theta$ oscillations disappear as $\sin 2\theta^m \to 0$. If V and $\cos 2\theta$ have the same sign, we get $\cos 2\theta^m \to -1$ and the mixing takes form:

$$\begin{pmatrix}\nu_\alpha\\ \nu_\beta\end{pmatrix} = \begin{pmatrix}0 & 1\\ -1 & 0\end{pmatrix}\begin{pmatrix}\nu_i\\ \nu_j\end{pmatrix} \tag{1.58}$$

On the contrary, if V and $\cos 2\theta$ have opposite signs, we get $\cos 2\theta^m \to +1$ and the mixing is:

$$\begin{pmatrix}\nu_\alpha\\ \nu_\beta\end{pmatrix} = \begin{pmatrix}1 & 0\\ 0 & 1\end{pmatrix}\begin{pmatrix}\nu_i\\ \nu_j\end{pmatrix} \tag{1.59}$$

Note that neutrinos and antineutrinos have opposite sign of V.

1.4.3 Oscillation parameters

Parameters that determine neutrino oscillations in three neutrino framework are three mixing angles (θ_{12}, θ_{13}, θ_{23}), one CP-violating phase (δ) and two of three square mass differences (Δm^2_{21}, Δm^2_{31}, Δm^2_{32}), the third one can be calculated from the other ones, e.g.: $\Delta m^2_{31} = \Delta m^2_{32} + \Delta m^2_{21}$.

Our current knowledge of the mass splitting and mixing angles stems from experiments measuring solar neutrinos (ν_e originating in solar thermonuclear reactions), reactor neutrinos ($\overline{\nu}_e$ produced in beta decays of neutron-rich nuclei originating in fission in nuclear reactors), atmospheric neutrinos produced in atmosphere when cosmic rays hit it (ν_μ, $\overline{\nu}_\mu$, ν_e, $\overline{\nu}_e$ as subsequent decay products of pions, muons, kaons etc.) and accelerator neutrinos (currently ν_μ, $\overline{\nu}_\mu$ from pion decays).

A certain combination of oscillation parameters is measured in each experiment.

Measurement of $\boldsymbol{\theta_{12}}$ and $\boldsymbol{\Delta m^2_{21}}$

Due to smallness of the θ_{13} angle, ν_e and $\overline{\nu}_e$ oscillations are mostly determined by θ_{12} and Δm^2_{21}. That allows us to calculate the survival probability up to a certain precision in the two neutrino approximation [8]:

$$P_{ee}(L/E) = 1 - \sin^2(2\theta_{sol}) \sin^2\left(\frac{\Delta m^2_{sol} L}{4E\hbar c}\right) \tag{1.60}$$

where we use effective parameters $\Delta m^2_{sol} \cong \Delta m^2_{21}$ and $\theta_{sol} \cong \theta_{21}$. The *sol* in subscript stands for "solar" as they determine the flux of solar ν_e that we observe. Since the diameter of solar core is much bigger than the oscillation length, we cannot observe particular oscillation cycles, only their average. Moreover, matter effect has to be considered as well. In the core of Sun, the condition $V = \cos 2\theta_{sol}$ is satisfied for energy $E_\nu = 1.45MeV$ [8]. Increasing energy further, we get to situation described by Eq. (1.58):

$$\begin{pmatrix} \nu_e \\ \nu_{\mu,\tau} \end{pmatrix} = \begin{pmatrix} 0 & 1 \\ -1 & 0 \end{pmatrix} \begin{pmatrix} \nu_1 \\ \nu_2 \end{pmatrix} \tag{1.61}$$

where ν_1 is assigned to the lighter mass eigenstate and ν_2 to the heavier. Neutrinos then leave sun in the heavier eigenstate ν_2 which has ν_e content of $\sin^2\theta_{sol}$ (about a third). On the contrary, neutrinos with energies $E_\nu < 0.5MeV$ [8] are rather unaffected and we observe mean oscillation value $1 - 0.5\sin^2(2\theta_{sol})$. Solar neutrinos were observed in Homestake, GALLEX, SAGE, SNO experiments, ν_e survival probabilities based on their results are shown in Fig. 1.1. Besides that, reactor $\overline{\nu}_e$ were also used for measurement of Δm^2_{21} and θ_{12} in KamLAND experiment.

It has been revealed that $\Delta m^2_{21} = (7.53 \pm 0.18) \cdot 10^{-5}\mathrm{eV}^2$ [10] (for summary of values of oscillation parameters see Tab. 1.1) which places the first disappearance minimum of ν_e and $\overline{\nu}_e$ to the distance of 16.4 km/MeV in vacuum. We know the sign of Δm^2_{21} thanks to effect of solar matter. For the mixing angle we have $\sin^2 2\theta_{12} = 0.85 \pm 0.02$ [10] which corresponds to $\theta_{12} \approx 33°$.

Measurement of $\boldsymbol{\theta_{23}}$ and $\boldsymbol{\Delta m^2_{32}}$

The gap that separates m^2_3 from m^2_2 and m^2_1 is about 33× bigger than the one that separates m^2_2 and m^2_1 so that it can be stated:

$$7.5 \cdot 10^{-5}\mathrm{eV}^2 \approx \Delta m^2_{sol} = \Delta m^2_{21} \ll |\Delta m^2_{31}| \cong |\Delta m^2_{32}| \cong |\Delta m^2_{atm}| \approx 2.5 \cdot 10^{-3}\mathrm{eV}^2 \tag{1.62}$$

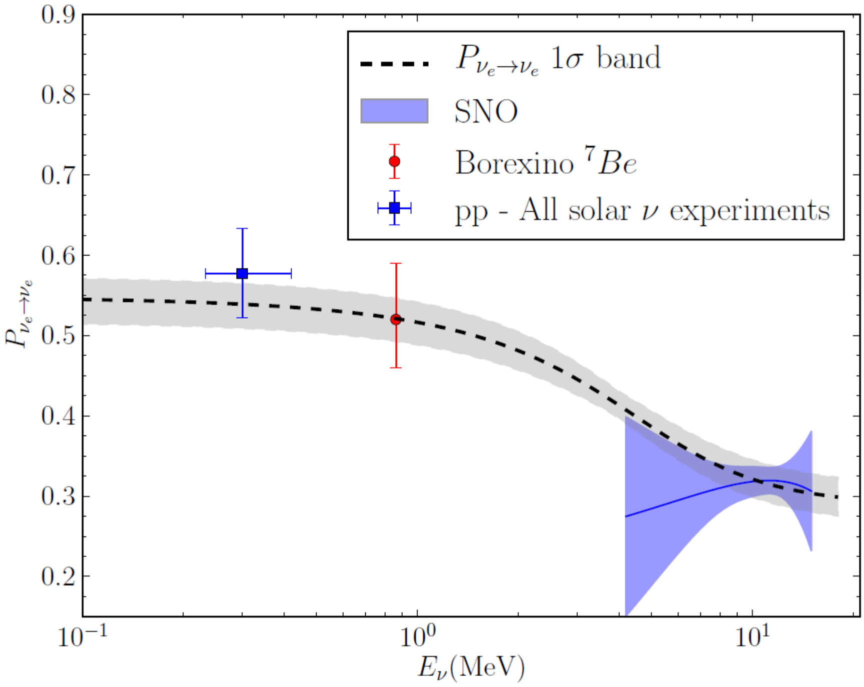

Figure 1.1: Survival probabilities of solar neutrinos: experimental results and prediction (dashed line). This figure was taken from [9].

The *atm* in subscript stands for "atmospheric" and it stems from the fact that oscillations driven by Δm^2_{32}, Δm^2_{31} play crucial role for atmospheric ν_μ and $\overline{\nu}_\mu$. They were first observed by Super-Kamiokande (SK-I) experiment and two neutrino framework was used with sufficient precision:

$$P_{\mu\mu}(L/E) = P_{\overline{\mu}\overline{\mu}}(L/E) = 1 - \sin^2(2\theta_{atm}) \sin^2\left(\frac{\Delta m^2_{atm} L}{4E\hbar c}\right) \tag{1.63}$$

Later, experiments measuring neutrinos of accelerator origin (K2K, T2K, MINOS(+)) complemented and eventually overcome the measurements of the atmospheric ones. However, the sign of Δm^2_{32} still remains unknown and the mass eigenstate ν_3 can be either the heaviest or the lightest one. The order of masses is called neutrino mass hierarchy. *Normal hierarchy* corresponds to $m^2_3 > m^2_2, m^2_1$, *inverted hierarchy* to $m^2_3 < m^2_2, m^2_1$. We shall look at it in detail in Chapter 2.

The fact that Δm^2_{32}, Δm^2_{31} are about 32× bigger than Δm^2_{21} while they differ only by Δm^2_{21} places the first disappearance minimum to about 0.5 km/MeV for both Δm^2_{32} and Δm^2_{31} driven oscillations.

Since $\sin^2 2\theta_{23} = 1.00 \pm 0.02$, the value of θ_{23} is around 45°, however it can be either $\theta_{23} < 45°$ or $\theta_{23} > 45°$. T2K experiment result is about 47° [11], in contrary to MINOS(+) results of approximately 39° or 51° [12]. The question of θ_{23} octant is yet to be resolved.

Measurement of θ_{13} and Δm^2_{31}

The angle θ_{13} is the last one that has been measured. There are currently two ways of measuring θ_{13}: reactor $\overline{\nu}_e$ disappearance (Daya Bay, Double Chooz, RENO) and ν_e ($\overline{\nu}_e$) appearance in ν_μ ($\overline{\nu}_\mu$) beam (MINOS, T2K), both driven by Δm^2_{32}

and Δm^2_{31}. The most precise result $\sin^2 2\theta_{13} = (8.41 \pm 0.33) \cdot 10^{-2}$ (the value of θ_{13} is about 8°) comes from Daya Bay experiment [13].

From the reactor $\overline{\nu}_e$ experiments, Daya Bay and RENO measure the square mass difference which is combination of Δm^2_{31} and Δm^2_{32} as we shall see later.

Measurement of δ-phase

According to global analysis of neutrino oscillation data [14] the best-fit value of δ-phase is around 1.3π, nevertheless all values are allowed within 3-σ region.

parameter	best-fit ($\pm 1\sigma$)
Δm^2_{21}	$(7.53 \pm 0.18) \cdot 10^{-5}\mathrm{eV}^2$
Δm^2_{32}	$(2.44 \pm 0.06) \cdot 10^{-3}\mathrm{eV}^2$ (normal hierarchy)
$\lvert\Delta m^2_{32}\rvert$	$(2.49 \pm 0.06) \cdot 10^{-3}\mathrm{eV}^2$ (inverted hierarchy)
$\sin^2 2\theta_{12}$	0.846 ± 0.021
$\sin^2 2\theta_{23}$	$0.999^{+0.001}_{-0.018}$ (normal hierarchy)
$\sin^2 2\theta_{23}$	$1.000^{+0.000}_{-0.017}$ (inverted hierarchy)
$\sin^2 2\theta_{13}$	0.0841 ± 0.0033

Table 1.1: Best fit values of neutrino oscillation parameters according to [10], except for $\sin^2 2\theta_{13}$ [13].

2. Neutrino mass hierarchy

As we have seen in previous chapter, along with the absolute value of Δm_{21}^2 we know that $m_2^2 > m_1^2$ due to the matter effects in Sun . The gap that separates m_3^2 from m_1^2 and m_2^2 is about 33× bigger than the one separating m_2^2 from m_1^2, but the sign of Δm_{32}^2 (Δm_{31}^2) is currently unknown. In other words: it is not clear whether ν_3 is the heaviest or the lightest mass eigenstate. The ordering of neutrino masses is called neutrino mass hierarchy.

There are two possible hierarchies:

- **Normal hierarchy** corresponds to $m_3^2 > m_2^2 > m_1^2$ ordering. It will be denoted "NH".
- **Inverted hierarchy** corresponds to $m_2^2 > m_1^2 > m_3^2$ ordering. It will be denoted "IH".

It is shown in Fig. 2.1 along with the fractional flavour content in each neutrino mass eigenstate. This content will be of particular importance later.

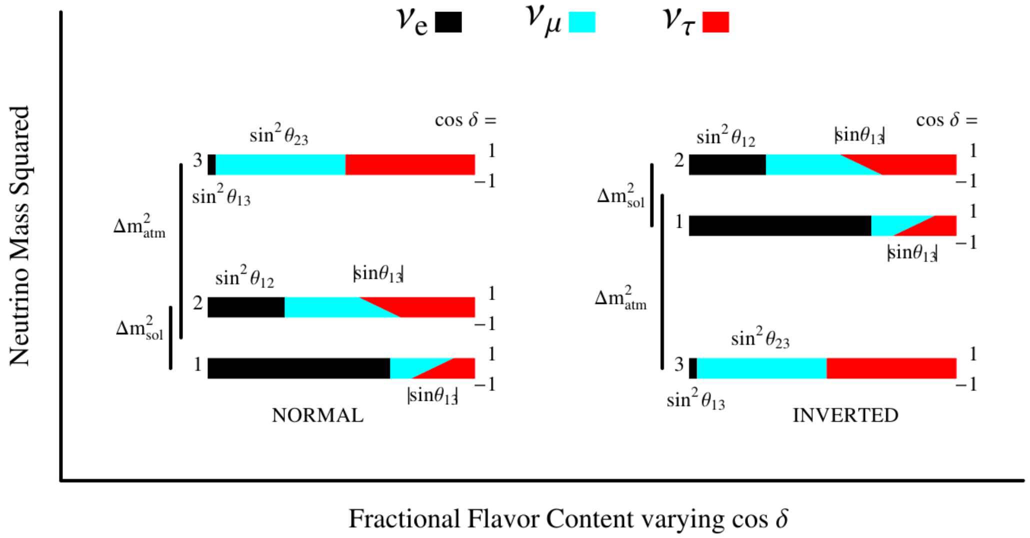

Figure 2.1: The flavour content in the neutrino mass eigenstates for both normal and inverted hierarchy as the CP-violating phase δ ($\cos\delta$) is varied. Coloured fractions denote the probability to find a corresponding neutrino flavour in the particular mass eigenstate. This figure was taken from [15].

2.1 Reasons to determine mass hierarchy

There are several reasons to determine neutrino mass hierarchy. Knowledge of mass hierarchy may support or disprove various theoretical models trying to explain neutrino masses and mixing. Other reasons that we shall discuss in more detail are the role of mass hierarchy in neutrinoless double β-decay and determination of CP-violating phase δ in neutrino oscillations.

2.1.1 Neutrinoless double β-decay

One of big questions concerning neutrinos is that whether they are Majorana or Dirac particles, i.e. whether neutrino is its own antiparticle or not. Majorana nature of neutrinos together with their non-zero masses would mean that there are neutrino processes that violate the total lepton number.

If neutrinos were massless, their chirality would coincide with helicity. Left-handed neutrinos produced together with positively charged lepton via CC interaction can only produce negatively charged lepton in subsequent interaction, regardless its nature. Analogically for (anti)neutrino produced with negatively charged lepton.

However, if neutrinos are massive, helicity corresponds to chirality only approximately and a small portion of "wrong" helicity (e.g. right-helicity neutrinos created along with positively charged lepton that act in subsequent reaction as right-handed) is present. If neutrinos are massive Majorana particles, this can lead to creation of lepton with opposite charge than we expect for zero mass or Dirac nature (e.g. while neutrino is created along with positively charged lepton, it interacts via CC resulting in creation of positively charged lepton again). Total lepton number is violated. Such processes are however suppressed by factor m_i^2/E^2 [1]. Considering neutrino masses $\lesssim 1\,\mathrm{eV}$ and energies $\gtrsim 1\,\mathrm{MeV}$, the factor m_i^2/E^2 does not exceed 10^{-12}.

Out of processes that stem from Majorana nature of neutrinos (if that is indeed true) and violate total lepton number, neutrinoless double β-decay ($0\nu\beta\beta$) is the most suitable one for experiments.

Let's consider an even-even nucleus with Z protons, A nucleons and mass $m(Z, A)$. Besides that, let's assume that due to the pairing energy in Weizsäcker formula:

$$m(Z, A) < m(Z + 1, A) \tag{2.1}$$

and simple β-decay is not possible. Nevertheless, it may still happen that

$$m(Z, A) > m(Z + 2, A) + 2m_e \tag{2.2}$$

where m_e denotes the electron mass. In such case, double β-decay occurs (albeit strongly suppressed). It can be viewed as two simultaneous β-decays of two nucleons, presumably in a form:

$$(Z, A) \to (Z + 2, A) + 2e^- + 2\overline{\nu}_e \tag{2.3}$$

which is denoted $2\nu\beta\beta$. Besides that, for massive Majorana neutrinos, following is in principle possible as well:

$$(Z, A) \to (Z + 2, A) + 2e^- \tag{2.4}$$

as neutrino is its own antiparticle. However, such process is strongly suppressed compared to Eq. (2.3). The decay rate is proportional to squared effective Majorana mass $m_{\beta\beta}^2$ which is defined [1]:

$$m_{\beta\beta} = |\sum_i U_{ei}^2 m_i| \tag{2.5}$$

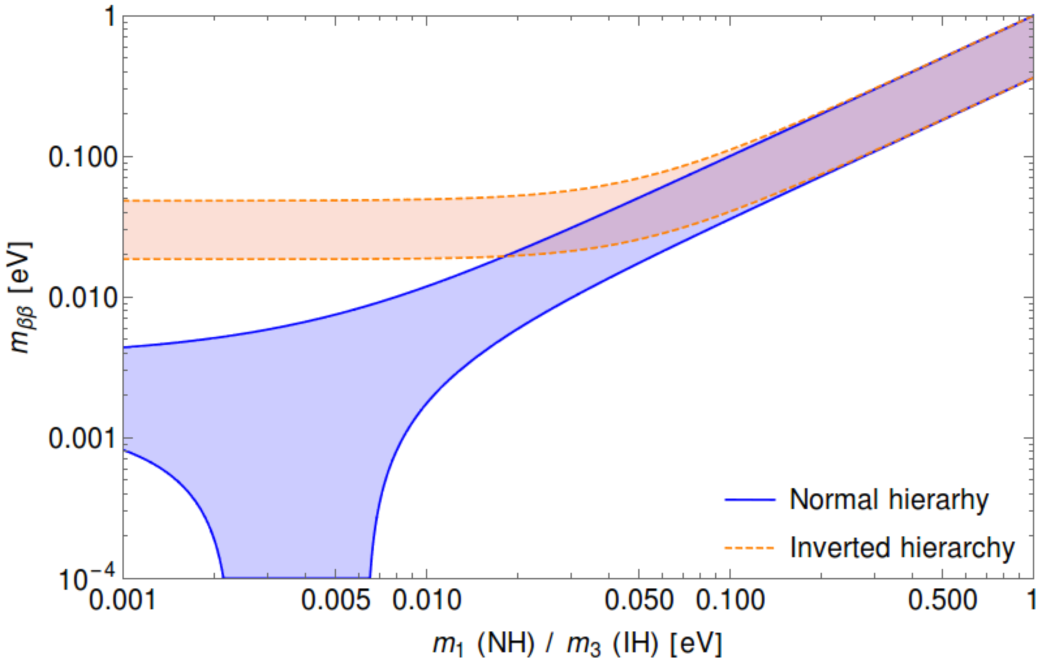

Figure 2.2: Effective Majorana mass $m_{\beta\beta}$ for NH and IH as a function of mass of the lightest mass eigenstate which is m_1 for NH and m_3 for IH. The values of Majorana phases α_1, α_2 are completely unknown, hence the intervals. Note that in case of NH the value of $m_{\beta\beta}$ may be zero for a certain values of m_1. On the contrary, in case of IH, there is lower bound $m_{\beta\beta} \geq 0.018$.

Unlike in case of neutrino oscillations, Majorana phases α_1, α_2 (see Eq. (1.36)) play crucial role here. As a result, we can predict only a range of $m_{\beta\beta}$ values for particular values of m_1, m_2 and m_3 within the particular mass hierarchy. This is shown in Fig. 2.2 as function of mass of the lightest mass eigenstate which is m_1 for NH and m_3 for IH.

The situation is different for NH and IH. Most remarkably, while for NH $m_{\beta\beta}$ may be zero for a certain values of m_1, for IH there is lower bound $m_{\beta\beta} \geq 0.018\,\text{eV}$ with parameter values listed in Table 1.1.

Observation of double beta decay with pursuit of $0\nu\beta\beta$ discovery has been carried out in several experiments: CUORICINO (observing ^{130}Te) [16], EXO (^{136}Xe) [17], GERDA (^{76}Ge) [18], KamLAND-Zen(^{136}Xe) [6], NEMO-3 (^{100}Mo) [19]. They provided only upper bounds for $m_{\beta\beta}$ so far; the most stringent one comes from KamLAND-Zen experiment and is $0.060 - 0.161\,\text{eV}$ at 90% CL depending on nuclear matrix element [6].

The next generation of experiments will naturally aim to reach $m_{\beta\beta}$ sensitivity that corresponds to IH area characterized by lower bound of about $0.018\,\text{eV}$ (see Fig. 2.2). Knowledge of neutrino mass hierarchy will be of particular importance at that point. If the result of $0\nu\beta\beta$ search is negative and NH holds, there is always possibility that $m_{\beta\beta}$ is smaller if not zero and no conclusion about neutrino nature (Dirac/Majorana) can be made. On the contrary, if IH holds, Majorana nature of neutrinos can be ruled out. If the result of $0\nu\beta\beta$ search is positive, different conclusions about absolute neutrino mass scale can be made for NH and IH along with establishing that neutrinos are Majorana particles.

2.1.2 Determination of CP-violating phase δ

Although there are in theory several ways of phase δ measurement, from practical point of view the opportunities are very limited. There is no source of ν_τ and $\overline{\nu}_\tau$ and their detection is a challenging task as well (both due to the threshold energy about 3.5 GeV needed to produce τ-lepton in CC interaction with nucleon and difficulty of its subsequent identification). Neither is there a pure source ν_e or $\overline{\nu}_e$ with sufficient energy to create μ-lepton (threshold 110 MeV for ν_μ). There are certain proposals that would overcome this deficiency such as beta beams [20] and neutrino factories [21] but only on paper so far.

Given these circumstances, only few possibilities remain:

- Comparison of mass splitting measured in reactor $\overline{\nu}_e \to \overline{\nu}_e$ and accelerator $\nu_\mu \to \nu_\mu$ disappearances. As we shall see in Chapter 3, information about $\cos\delta$ may be obtained this way but precision beyond reach of currently running experiments would be required.

- Comparison of accelerator $\nu_\mu \to \nu_e$ and $\overline{\nu}_\mu \to \overline{\nu}_e$ appearances. Here, matter effect dependent on mass hierarchy creates ambiguity when an experimental result might suggest one value of δ for NH and a different one for IH. It is illustrated by expected oscillation probabilities for NOνA experiment in Fig. 2.3.

- Comparison of reactor $\overline{\nu}_e \to \overline{\nu}_e$ disappearance and accelerator $\nu_\mu \to \nu_e$ appearance. The formula describing $P_{\mu e}$ is rather complicated (for explicit form see [22, 23]). It is sensitive to $\sin 2\theta_{13}$, δ, octant of θ_{23} and mass hierarchy via matter effects. When compared with $\sin 2\theta_{13}$ from reactor antineutrino experiments, restrictions concerning value of δ depending on mass hierarchy can be made. This is illustrated in Fig. 2.4.

2.2 Determination of the mass hierarchy

When we consider vacuum oscillation driven by a single square mass difference $\mathrm{Re}[U^*_{\alpha i}U_{\beta i}U_{\alpha j}U^*_{\beta j}]\sin^2\left(\frac{\Delta m^2_{ij}L}{4E\hbar c}\right)$, we see that the sign of Δm^2_{ij} is of no importance, the result is the same for either. The sign of Δm^2_{ij} becomes important when the effect of matter is no longer negligible as we have seen in Chapter 1. Neutrino transition through sun matter has already provided us with the fact that $\Delta m^2_{21} > 0$. Likewise, matter effect can be used to determine the sign of Δm^2_{31}. It is not very important for reactor $\overline{\nu}_e$ but as its influence grows with neutrino energy E (and electron density), it plays a significant role for ν_μ and $\overline{\nu}_\mu$ beams and ν_e and $\overline{\nu}_e$ appearance in them, atmospheric and supernova neutrinos:

- **Accelerator neutrinos:** As we have discussed in the section about CP-violating phase δ determination, both mass hierarchy through matter effect and phase δ contribute to ν_e and $\overline{\nu}_e$ appearance probabilities which may

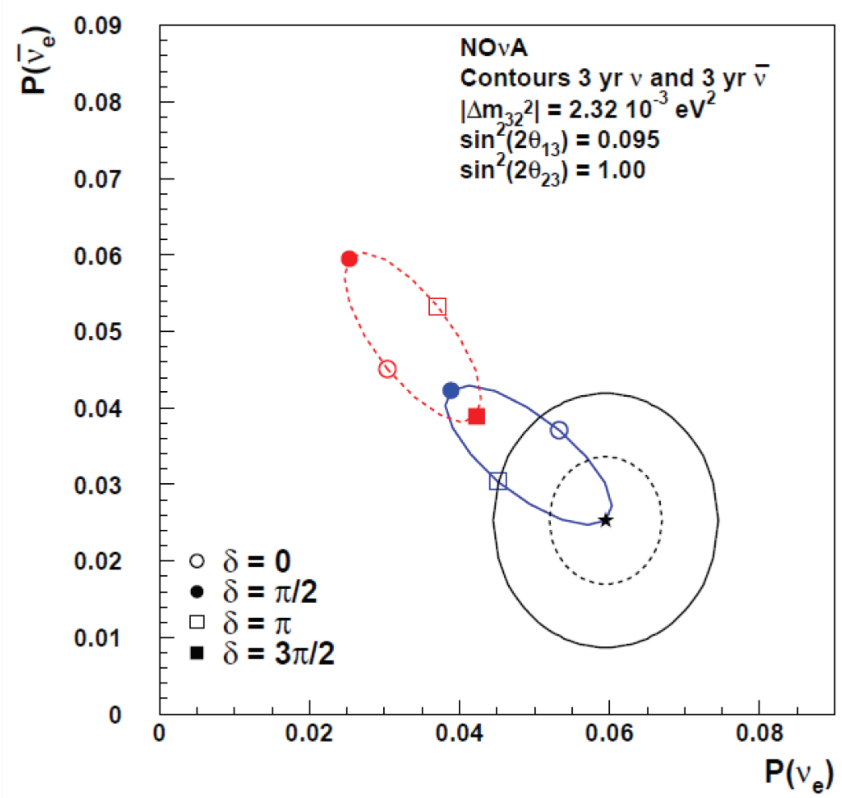

Figure 2.3: Expected oscillation probabilities for $\nu_\mu \to \nu_e$ and $\overline{\nu}_\mu \to \overline{\nu}_e$ in NOνA experiment for various scenarios. The solid blue ellipse corresponds to NH, dashed blue to IH. When varying δ, one moves around an ellipse. We can see that for example $\delta = \pi/2$ and NH yields similar result to $\delta = \pi/2$ and IH. This figure was taken from [24]

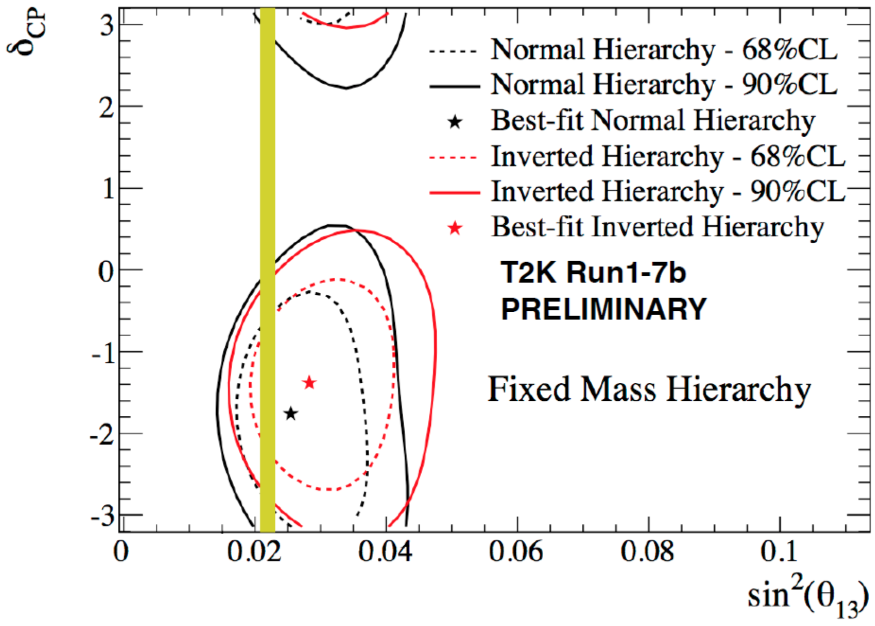

Figure 2.4: The $\nu_\mu \to \nu_e$ appearance contour shown as a function of $\sin^2 2\theta_{13}$ and δ from T2K experiment. The vertical strip represents 1σ area of reactor antineutrino results. This figure was taken from [11].

cause ambiguities. Nevertheless, combination of results from accelerator neutrino experiments and reactor antineutrino experiments (as shown in Fig. 2.4) has already provided some evidence about mass hierarchy preference. The most precise accelerator neutrino experiment is T2K; combination of its results with those of reactor antineutrino experiments (most notably Daya Bay) led to $\delta \in [-3.02, -0.49]$ for NH and $\delta \in [-1.87, -0.98]$ for IH at 90% CL, overall favouring NH at 74.7% [11].

- **Atmospheric neutrinos:** Atmosphere is an important source of neutrinos on GeV scale (ν_μ, $\overline{\nu}_\mu$, ν_e, $\overline{\nu}_e$ produced there when cosmic rays hit the atmosphere). The influence of matter effect on oscillations grows as the zenith angle increases and neutrinos pass longer distances through denser layers of Earth. Thus their observation may provide evidence concerning mass hierarchy. Since the oscillations patterns for neutrinos and antineutrinos exchange with exchange of NH $\leftrightarrow$ IH, identification of lepton (in practice muon) charge[1] would be desirable (for more information see [23]). Nonetheless, results of observation of atmospheric neutrinos in Super-Kamiokande experiment show preference for NH, both alone and in combination with T2K results [25].

- **Supernova neutrinos:** Mass hierarchy via matter effect plays also important role for neutrinos originating in core-collapse supernovae. However, it is a very complicated matter (including such phenomena as collective oscillations of neutrinos), far beyond scope of this thesis.

Another approach to neutrino mass hierarchy problem is to conduct measurement precise enough to distinguish oscillation pattern caused by different contributions of Δm^2_{31} and Δm^2_{32} driven oscillations. Such pattern is different for NH and IH. The JUNO experiment, currently under construction, is designed to perform such measurement with reactor $\overline{\nu}_e$. We shall look at it in more detail in the next section. RENO-50 is a similar project located in South Korea that has been proposed.

The last way of determination of neutrino mass hierarchy we shall discuss is based on comparison of the mass splitting measured in reactor $\overline{\nu}_e$ and accelerator ν_μ disappearances. Since investigation of this approach is one of the main aims of this thesis, it will be discussed in detail in Chapter 3.

2.2.1 JUNO experiment

JUNO stands for Jiangmen Underground Neutrino Observatory [26, 27]. Located in Jiangmen city in Guangdong province in China, it is 53 km from Taishan and Yangjiang nuclear power plants (the distance is chosen in order to have the best sensitivity for the mass hierarchy determination). Currently, it is under construction; start of data taking is expected in 2020.

The placement of the JUNO detector is 700 m underground. The scheme is shown in Fig. 2.5. The central detector is spherical and contains 20 kton of liquid scintillator with attenuation length $\geq 20\,\mathrm{m}$. The light is collected by $\sim 17,000$ PMTs covering $\geq 75\%$ of the surface. This detector is submerged in a

---

[1] charge of lepton produced in neutrino CC interaction

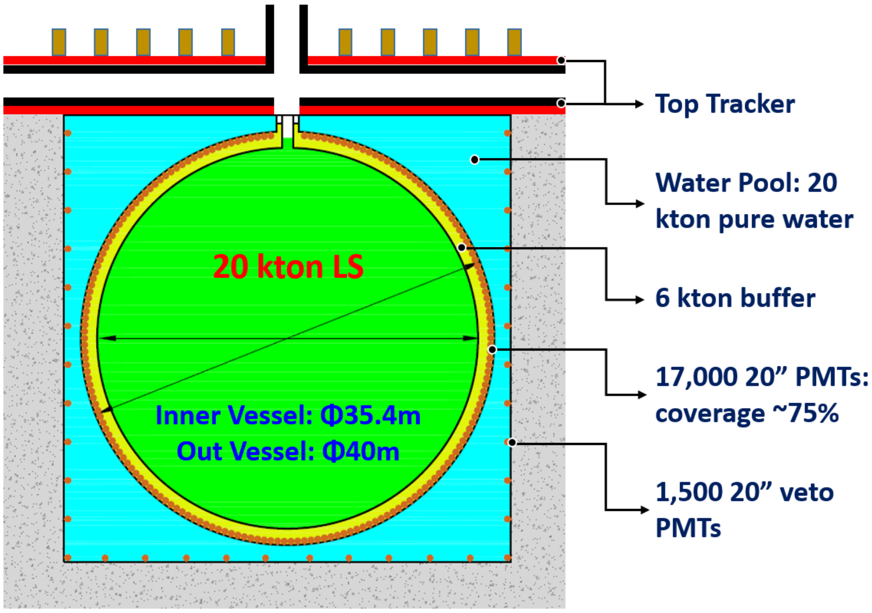

Figure 2.5: Scheme of the JUNO detector. This figure was taken from [27].

water pool which is equipped with $\sim 1,500$ PMTs in order to detect Cherenkov light emitted by cosmic muons. On the top of the pool is another detector for muon tracking. RPCs were considered as an option (results of measurement of Daya Bay type RPC properties are in Chapter 4), but as OPERA detector is to be dismounted, its target tracker made of scintillating strips will be used instead.

Neutrinos ($\overline{\nu}_e$) will be observed using inverse beta decay (IBD) $\overline{\nu}_e + p \rightarrow e^+ + n$ with threshold of 1.8 MeV. Positron created in IBD loses energy and eventually annihilates creating the prompt signal. Delayed signal is produced by neutron capture on nucleus (mostly hydrogen in JUNO).

The goal is to achieve $3\%/\sqrt{E(MeV)}$ energy resolution in order to recognize the oscillation pattern and eventually determine the neutrino mass hierarchy. This is demonstrated in Fig. 2.6. In the upper part, there is expected neutrino spectrum in case NH is the true hierarchy and the best fit for IH (wrong hierarchy in this case). In the lower part, ratio of these two is shown. Besides that, $\sin^2\theta_{12}$, Δm^2_{21}, $|\Delta m^2_{ee}|$ will be measured with precision better than 1% by JUNO experiment.

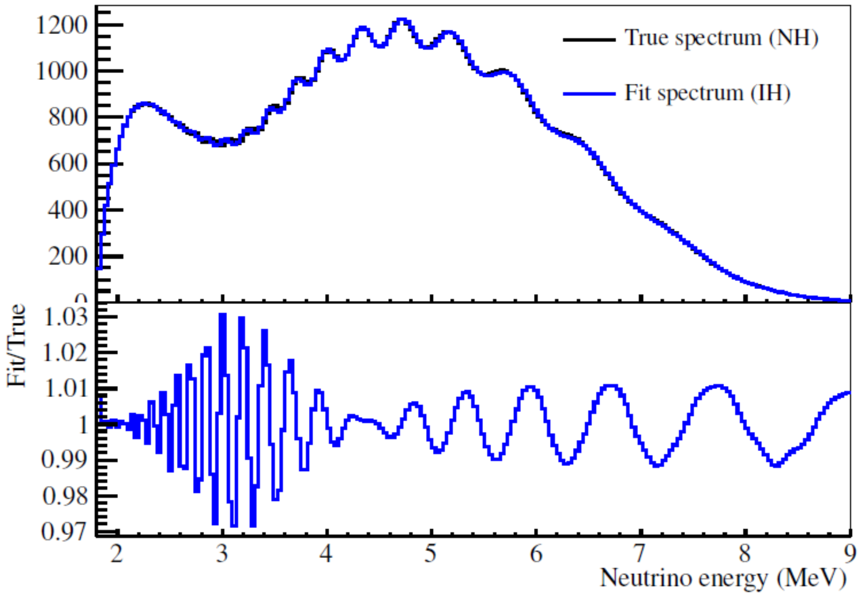

Figure 2.6: The expected $\overline{\nu}_e$ spectrum in case that NH is the true one and IH fit are shown in the upper part, their ratio in the lower one. This figure was taken from [27].

3. Neutrino mass hierarchy determination by comparison of mass splitting

In this chapter, we shall look at the possibility of mass hierarchy determination by comparison of mass splitting measured in reactor and accelerator neutrino experiments. This can be done by comparison of Δm^2_{ee} with $\Delta m^2_{\mu\mu}$ (this approach is also elaborated in [28]) or by comparison of m^2_{32} from multiple experiments.

As it is shown in Fig. 2.1, every flavour eigenstate is present in each of the mass eigenstates. As a result, we never observe oscillations driven solely by Δm^2_{31} or Δm^2_{32}; we can observe only their combinations.

3.1 Approximation using $\Delta m^2_{\alpha\alpha}$

Let's focus now on the survival probability of a particular flavour α, i. e. disappearance experiments. One can derive such probability as a special case of Eq (1.44):

$$P_{\alpha\alpha} = 1 - 4|U_{\alpha 2}|^2|U_{\alpha 1}|^2 \sin^2\left(\frac{\Delta m^2_{21}L}{4E\hbar c}\right) - \\ - 4|U_{\alpha 3}|^2\left(|U_{\alpha 1}|^2\sin^2\left(\frac{\Delta m^2_{31}L}{4E\hbar c}\right) + |U_{\alpha 2}|^2\sin^2\left(\frac{\Delta m^2_{32}L}{4E\hbar c}\right)\right) \quad (3.1)$$

The difference between Δm^2_{31} and Δm^2_{32} is only about 3% ($|\Delta m^2_{31} - \Delta m^2_{32}| = \Delta m^2_{21}$). This fact allows us to use following approximation with sufficient precision when dealing with first oscillation cycle:

$$P_{\alpha\alpha} \cong 1-4|U_{\alpha 2}|^2|U_{\alpha 1}|^2\sin^2\left(\frac{\Delta m^2_{21}L}{4E\hbar c}\right)-4|U_{\alpha 3}|^2\left(|U_{\alpha 1}|^2+|U_{\alpha 2}|^2\right)\sin^2\left(\frac{\Delta m^2_{\alpha\alpha}L}{4E\hbar c}\right) \quad (3.2)$$

where

$$\Delta m^2_{\alpha\alpha} = \left|\frac{|U_{\alpha 1}|^2}{|U_{\alpha 1}|^2+|U_{\alpha 2}|^2}\Delta m^2_{31} + \frac{|U_{\alpha 2}|^2}{|U_{\alpha 1}|^2+|U_{\alpha 2}|^2}\Delta m^2_{32}\right| \quad (3.3)$$

The purpose of this approximation is to replace two distinct oscillations driven by Δm^2_{31} and Δm^2_{32} with one oscillation driven by $\Delta m^2_{\alpha\alpha}$:

$$\frac{|U_{\alpha 1}|^2}{|U_{\alpha 1}|^2+|U_{\alpha 2}|^2}\sin^2\left(\frac{\Delta m^2_{31}L}{4E\hbar c}\right) + \frac{|U_{\alpha 2}|^2}{|U_{\alpha 1}|^2+|U_{\alpha 2}|^2}\sin^2\left(\frac{\Delta m^2_{32}L}{4E\hbar c}\right) \cong \\ \cong \sin^2\left(\frac{\Delta m^2_{\alpha\alpha}L}{4E\hbar c}\right) \quad (3.4)$$

The comparison of the exact oscillation probability and the approximation is shown in Fig. 3.1. In general, the approximation is least precise for $|U_{\alpha 1}|^2 \simeq |U_{\alpha 2}|^2$, nevertheless, the difference between left and right side of the formula (3.4) is $\lesssim 0.06\%$ in the distance of the first disappearance minimum for any ratio of

$|U_{\alpha 1}|^2$ and $|U_{\alpha 2}|^2$. On the contrary, parameters defining $|U_{\alpha i}|^2$ are measured with precision $\gtrsim 2\%$ nowadays.

The shift in the position of the first disappearance minimum due to the approximation is equivalent to the shift of $\Delta m^2_{\alpha\alpha}$ by $\lesssim 0.05\%$, whereas the precision of the mass-splitting measurement is currently $\gtrsim 2\%$.

From the described precision of the approximation we can conclude that the approximation is valid for recent experiments measuring the first oscillation cycle driven by combination of Δm^2_{31} or Δm^2_{32}.

3.2 Difference between Δm^2_{ee} and $\Delta m^2_{\mu\mu}$

From Eq. (3.3) we see that $\Delta m^2_{\alpha\alpha}$ is in fact an average between Δm^2_{31} and Δm^2_{32} weighted by the fraction of ν_α present in ν_1 and ν_2 respectively. Since these fractions are generally different for various flavours[1], the exact value of $\Delta m^2_{\alpha\alpha}$ is also different for various flavours.

Since there are no experiments using ν_τ as the initial flavour, from now on we shall focus only on Δm^2_{ee} and $\Delta m^2_{\mu\mu}$. Using Eq. (1.37) (with its notation $s^2_{ij} \equiv \sin^2\theta_{ij}$, $c^2_{ij} \equiv \cos^2\theta_{ij}$) and (3.3) we get:

$$\Delta m^2_{ee} = |c^2_{12}\Delta m^2_{31} + s^2_{12}\Delta m^2_{32}| \tag{3.5}$$

$$\begin{aligned}\Delta m^2_{\mu\mu} = |\frac{1}{(1-s^2_{23}c^2_{13})}[c^2_{23}(s^2_{12}\Delta m^2_{31} + c^2_{12}\Delta m^2_{32}) + \\ + s^2_{23}s^2_{13}(c^2_{12}\Delta m^2_{31} + s^2_{12}\Delta m^2_{32}) + 2s_{12}c_{12}s_{23}c_{23}s_{13}\cos\delta(\Delta m^2_{31} - \Delta m^2_{32})]|\end{aligned} \tag{3.6}$$

Note that Δm^2_{ee} and $\Delta m^2_{\mu\mu}$ are always positive due to the absolute value in our definition.

It holds that for NH: $|\Delta m^2_{31}| > |\Delta m^2_{32}|$ and for IH: $|\Delta m^2_{31}| < |\Delta m^2_{32}|$. Since Δm^2_{ee} is closer to Δm^2_{31} and $\Delta m^2_{\mu\mu}$ is closer to Δm^2_{32}, we get $\Delta m^2_{ee} > \Delta m^2_{\mu\mu}$ for NH and $\Delta m^2_{ee} < \Delta m^2_{\mu\mu}$ for IH. The difference is:

$$\begin{aligned}\Delta m^2 \equiv \Delta m^2_{ee} - \Delta m^2_{\mu\mu} = \\ = \pm\frac{1}{(1+\tan^2\theta_{23}\sin^2\theta_{13})}(\cos 2\theta_{12} - \sin 2\theta_{12}\tan\theta_{23}\sin\theta_{13}\cos\delta)\Delta m^2_{21} \cong \\ \cong \pm(\cos 2\theta_{12} - \sin 2\theta_{12}\tan\theta_{23}\sin\theta_{13}\cos\delta)\Delta m^2_{21}\end{aligned} \tag{3.7}$$

where Δm^2 has positive sign in case of NH and negative in case of IH. The precision of the approximation (neglecting the term proportional to $\sin^2\theta_{13}$) in Eq. (3.7) is about 2%; we shall use the exact form for further calculations.

We can also write the relation between Δm^2_{ee} and $\Delta m^2_{\mu\mu}$ in the following form: $\Delta m^2_{ee} = \Delta m^2_{\mu\mu} + |\Delta m^2|$ for NH and $\Delta m^2_{ee} = \Delta m^2_{\mu\mu} - |\Delta m^2|$ for IH.

The value of $|\Delta m^2| = |\Delta m^2_{ee} - \Delta m^2_{\mu\mu}|$ as a function of $\cos\delta$ is drawn in Fig. 3.2. Since the value of CP-violating phase δ is not yet precisely determined (any value is allowed within 3σ interval), for $\theta_{23} = 45°$ the range of $|\Delta m^2|$ values stretches

---

[1] According to our current knowledge of PMNS matrix parameters, there is still possibility that ν_μ and ν_τ share the same fractional content in ν_1 and ν_2. It would require $\theta_{23} = 45°$ and $\delta = 90°$ or $270°$.

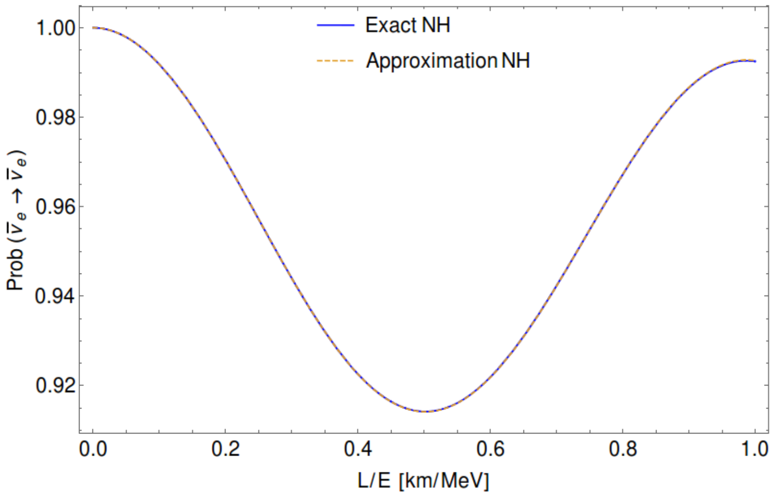

(a) First cycle

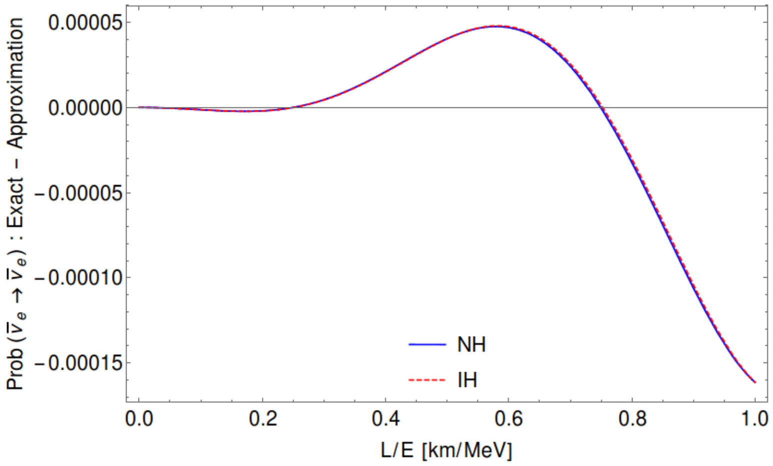

(b) Detail

Figure 3.1: The approximation using Δm^2_{ee} for the first cycle of $\overline{\nu}_e \to \overline{\nu}_e$ oscillations: in the upper figure both exact oscillation probability (solid blue line) and the approximation (dashed orange line) are drawn. Slow oscillations driven by Δm^2_{21} are the same for both. Note that the lines blend together. In the lower figure, difference between exact probability and approximation is drawn, solid blue line denoting NH and dashed red line IH. Oscillation parameters listed in Table 1.1 were used.

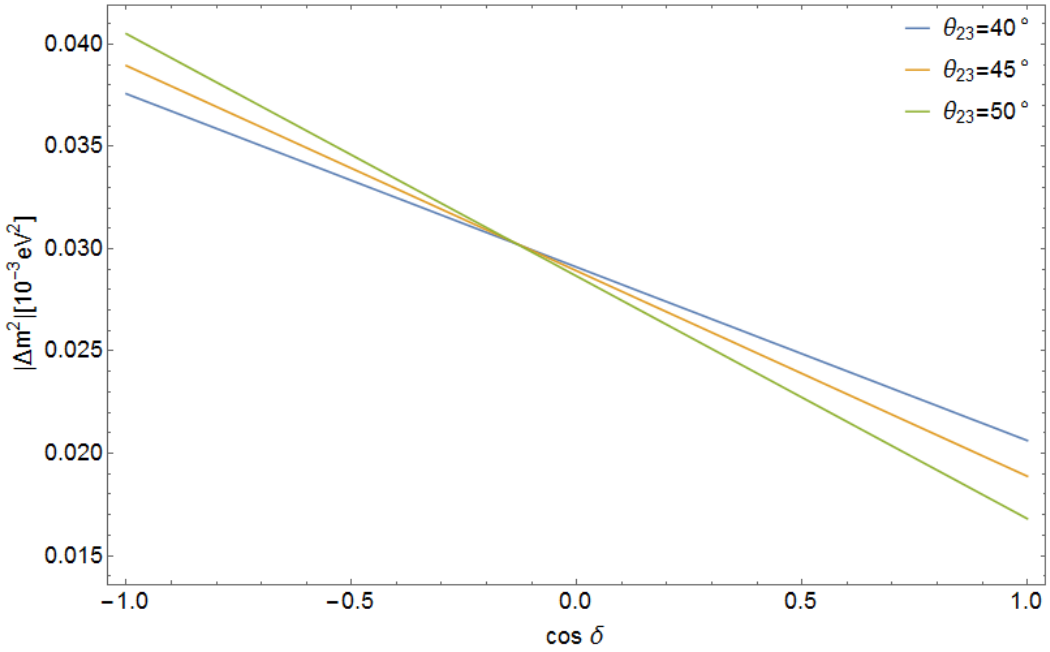

Figure 3.2: $|\Delta m^2| = |\Delta m^2_{ee} - \Delta m^2_{\mu\mu}|$ as a function of $\cos\delta$ for three distinct values of θ_{23}. All the other parameters were taken from Table 1.1.

from approximately $0.019 \cdot 10^{-3}\,\mathrm{eV}^2$ for $\delta = 0°$ to $0.039 \cdot 10^{-3}\,\mathrm{eV}^2$ for $\delta = 180°$. The presence of $\tan\theta_{23}$ terms makes Δm^2 sensitive to the octant of θ_{23}, mainly enhancing ($\theta_{23} > 45°$) or suppressing ($\theta_{23} < 45°$) the effect of $\cos\delta$ dependence.

This dependence of $|\Delta m^2|$ on $\cos\delta$ also means that precise measurement of Δm^2_{ee} and $\Delta m^2_{\mu\mu}$ can be used, in principle, to determine the value of $\cos\delta$. Current experiments measure Δm^2_{ee} and $\Delta m^2_{\mu\mu}$ with uncertainties of $0.08 \cdot 10^{-3}\,\mathrm{eV}^2$ or worse (Daya Bay [13], T2K [11], MINOS+ [12], NOνA [29], RENO [30]) which is too big for this purpose. However, precisions planned in JUNO [27] and DUNE/LBNF [31] are $0.013 \cdot 10^{-3}\,\mathrm{eV}^2$ and $0.004 \cdot 10^{-3}\,\mathrm{eV}^2$ respectively, which is enough to get some restrictions on $\cos\delta$ value, but with far less significance than other approaches described in Chapter 2.

3.3 Mass hierarchy determination

We saw that the mass hierarchy determines the relation between Δm^2_{ee} and $\Delta m^2_{\mu\mu}$, now we shall discuss how this can be used for the neutrino mass hierarchy problem along with using Δm^2_{32} measurements. We shall use and discuss three approaches:

- **Method 1** is based on the sign of $\Delta m^2 = \Delta m^2_{ee} - \Delta m^2_{\mu\mu}$ where Δm^2_{ee} and $\Delta m^2_{\mu\mu}$ are experimental results.
- **Method 2** is also based on $\Delta m^2 = \Delta m^2_{ee} - \Delta m^2_{\mu\mu}$ where Δm^2_{ee} and $\Delta m^2_{\mu\mu}$ are experimental results, but this time we shall compare it with theoretical value of Δm^2 calculated above.

- **Method 3** is based on comparison of Δm^2_{32} values measured in accelerator and reactor (anti)neutrino experiments.

3.3.1 Method 1 based on the sign of $\Delta m^2 = \Delta m^2_{ee} - \Delta m^2_{\mu\mu}$

We know that for NH it holds that $\Delta m^2 = \Delta m^2_{ee} - \Delta m^2_{\mu\mu} > 0$ and for IH $\Delta m^2 = \Delta m^2_{ee} - \Delta m^2_{\mu\mu} < 0$. If we are given results from experiments measuring Δm^2_{ee} and $\Delta m^2_{\mu\mu}$, we can calculate corresponding Δm^2 and the probabilities that it is > 0 and < 0.

Let's assume that there is an experiment measuring Δm^2_{ee} (and another one measuring $\Delta m^2_{\mu\mu}$) and it provides us with the mean value ΔM^2_{ee} ($\Delta M^2_{\mu\mu}$) and standard deviation σ_e (σ_μ). Assuming Gauss distribution, the value of Δm^2_{ee} ($\Delta m^2_{\mu\mu}$) is described by following probability density:

$$p(\Delta m^2_{ee}) = \frac{1}{\sigma_e\sqrt{2\pi}} e^{-\frac{(\Delta m^2_{ee} - \Delta M^2_{ee})^2}{2\sigma_e^2}}, \quad p(\Delta m^2_{\mu\mu}) = \frac{1}{\sigma_\mu\sqrt{2\pi}} e^{-\frac{(\Delta m^2_{\mu\mu} - \Delta M^2_{\mu\mu})^2}{2\sigma_\mu^2}} \tag{3.8}$$

Using these results, we can calculate Δm^2; it is again described by Gauss distribution:

$$p(\Delta m^2) = \frac{1}{\sqrt{2\pi(\sigma_e^2 + \sigma_\mu^2)}} e^{-\frac{(\Delta m^2 - (\Delta M^2_{ee} - \Delta M^2_{\mu\mu}))^2}{2(\sigma_e^2 + \sigma_\mu^2)}} \tag{3.9}$$

We get the probability of IH ($P(IH)$) by integrating Eq. (3.9) from $-\infty$ to 0 (the region where the sign of Δm^2 is negative) and analogically for the probability of NH ($P(NH)$):

$$P(NH) = \int_{-\infty}^{0} \frac{1}{\sqrt{2\pi(\sigma_e^2 + \sigma_\mu^2)}} e^{-\frac{(\Delta m^2 - (\Delta M^2_{ee} - \Delta M^2_{\mu\mu}))^2}{2(\sigma_e^2 + \sigma_\mu^2)}} \mathrm{d}\Delta m^2 \tag{3.10}$$

$$P(IH) = \int_{0}^{\infty} \frac{1}{\sqrt{2\pi(\sigma_e^2 + \sigma_\mu^2)}} e^{-\frac{(\Delta m^2 - (\Delta M^2_{ee} - \Delta M^2_{\mu\mu}))^2}{2(\sigma_e^2 + \sigma_\mu^2)}} \mathrm{d}\Delta m^2 \tag{3.11}$$

The principle of this approach is outlined in Fig. 3.3.

3.3.2 Method 2 based on the theoretical value of $\Delta m^2 = \Delta m^2_{ee} - \Delta m^2_{\mu\mu}$

In *Method 1* we only used the fact that $\Delta m^2 = \Delta m^2_{ee} - \Delta m^2_{\mu\mu} > 0$ for NH and $\Delta m^2 = \Delta m^2_{ee} - \Delta m^2_{\mu\mu} < 0$ for IH. However, using Eq. 3.7 we can calculate what the absolute value $|\Delta m^2|$ should be based on our knowledge of oscillation parameters. We shall denote this theoretical value $|\Delta m^2_t|$. For NH, we expect $\Delta m^2 = +|\Delta m^2_t|$ and for IH $\Delta m^2 = -|\Delta m^2_t|$. Since we already have described the distribution of Δm^2 in Eq. (3.9), we can now look how likely is each case, i.e. $\Delta m^2 = \pm|\Delta m^2_t|$. If we knew the precise value $|\Delta m^2_t|$, it would be:

$$L_\pm = \frac{1}{\sqrt{2\pi(\sigma_e^2 + \sigma_\mu^2)}} e^{-\frac{(\pm|\Delta m^2_t| - (\Delta M^2_{ee} - \Delta M^2_{\mu\mu}))^2}{2(\sigma_e^2 + \sigma_\mu^2)}} \tag{3.12}$$

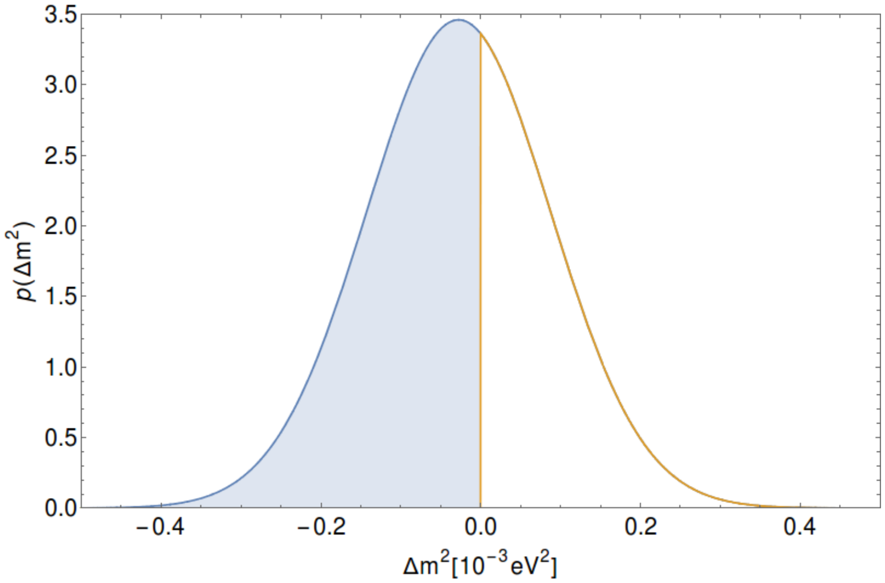

Figure 3.3: Illustration of *Method 1*. For this purpose, Δm^2_{ee} was taken from Daya Bay results [13] and $\Delta m^2_{\mu\mu}$ is considered to be mean value of Δm^2_{32} (NH) and Δm^2_{32} (IH) from T2K results [11]. Corresponding $\Delta m^2 = \Delta m^2_{ee} - \Delta m^2_{\mu\mu}$ distribution is shown. The blue area corresponds to negative sign of Δm^2 and IH, the rest corresponds to positive sign of Δm^2 and NH. Due to the uncertainties in measurements the Gauss function describing Δm^2 is quite wide compared to the offset of its peak position.

However, $|\Delta m_t^2|$ depends on parameters that are not known precisely ($\cos\delta$ in the first place). Therefore, $prob(|\Delta m^2|)$ that describes probability density of $|\Delta m_t^2|$ based on Eq. (3.7) and our knowledge of oscillation parameters needs to be determined. Using that, we get:

$$\tilde{L}_\pm = \int_0^\infty \frac{1}{\sqrt{2\pi(\sigma_e^2+\sigma_\mu^2)}} e^{-\frac{(\pm|\Delta m^2|-(\Delta M_{ee}^2-\Delta M_{\mu\mu}^2))^2}{2(\sigma_e^2+\sigma_\mu^2)}} prob(|\Delta m^2|)\mathrm{d}|\Delta m^2| \tag{3.13}$$

Using these results, we get the probability ratio of the NH vs. IH:

$$\frac{P(NH)}{P(IH)} = \frac{\tilde{L}_+}{\tilde{L}_-} \tag{3.14}$$

And both probabilities:

$$P(NH) = \frac{\tilde{L}_+}{\tilde{L}_+ + \tilde{L}_-} \tag{3.15}$$

$$P(IH) = \frac{\tilde{L}_-}{\tilde{L}_+ + \tilde{L}_-} \tag{3.16}$$

3.3.3 Method 3 based on comparison of Δm_{32}^2 measurements

Since accelerator neutrino experiments provide the latest results (presented at *Neutrino 2016* conference) in the form of Δm_{32}^2 for NH and IH and reactor antineutrino experiments provide both Δm_{ee}^2 and Δm_{32}^2 for NH and IH, it is logical to approach the task of mass hierarchy determination by comparing Δm_{32}^2 results from these experiments.

For that purpose, we calculate the (weighted) average of Δm_{32}^2 (NH) and Δm_{32}^2 (IH) from results of experiments. Then we can take this average for NH and using it we calculate how likely it is to obtain the set of experimental results we have. That way we get the likelihood $L(NH)$. We do the same for IH and get $L(IH)$. Comparing it, we calculate the probability of NH and IH:

$$P(NH) = \frac{L(NH)}{L(NH) + L(IH)} \tag{3.17}$$

$$P(IH) = \frac{L(IH)}{L(NH) + L(IH)} \tag{3.18}$$

For the wrong hierarchy, we expect that the Δm_{32}^2 experimental results will be spread more widely, making probability of the wrong hierarchy lower.

We can apply this procedure for just a pair of measurements (presumably one using reactor and the other one accelerator (anti)neutrinos) as well, it is useful to illustrate how the probabilities change with measurement precision. Let's denote the mean value of $|\Delta m_{32}^2|$ provided by a reactor antineutrino experiment ΔM_{eN}^2 (ΔM_{eI}^2) for NH (IH) and the standard deviation σ_e. Analogically for an accelerator neutrino experiment we have $\Delta M_{\mu N}^2$, $\Delta M_{\mu I}^2$, σ_μ. Then the probabilities are:

$$P(NH) = = \frac{1}{1+e^{\frac{(\Delta M^2_{eN}-\Delta M^2_{\mu N})^2-(\Delta M^2_{eI}-\Delta M^2_{\mu I})^2}{2(\sigma_e^2+\sigma_\mu^2)}}} \tag{3.19}$$

$$P(IH) = = \frac{1}{1+e^{-\frac{(\Delta M^2_{eN}-\Delta M^2_{\mu N})^2-(\Delta M^2_{eI}-\Delta M^2_{\mu I})^2}{2(\sigma_e^2+\sigma_\mu^2)}}} \tag{3.20}$$

3.3.4 Experimental results

There are 3 short-baseline experiments that measure $\overline{\nu}_e$ disappearance: Daya Bay, RENO and Double Chooz, but at the moment only Daya Bay and RENO provide measurement of Δm^2_{ee} and corresponding values of Δm^2_{32} (NH) and Δm^2_{32} (IH). The relation between Δm^2_{ee} and Δm^2_{32} (NH/IH) can be easily obtained by using Eq. (3.5):

$$\Delta m^2_{32} = \Delta m^2_{ee} - c^2_{12}\Delta m^2_{21}\ (NH), \quad |\Delta m^2_{32}| = \Delta m^2_{ee} + c^2_{12}\Delta m^2_{21}\ (IH) \tag{3.21}$$

The disappearance of ν_μ ($\overline{\nu}_\mu$) is most precisely measured by T2K, MINOS(+) and NOνA experiments. In newest analyses they fit Δm^2_{32} for both NH and IH rather than $\Delta m^2_{\mu\mu}$.

For our analysis, we shall use the newest results that were presented at *Neutrino 2016* conference. The values are listed in Table 3.1.

Experiment	Δm^2_{32} (NH) [10^{-3}eV^2]	$\lvert\Delta m^2_{32}\rvert$ (IH) [10^{-3}eV^2]
Daya Bay	2.45 ± 0.08	2.55 ± 0.08
RENO	2.57 ± 0.26	2.67 ± 0.26
T2K	2.51 ± 0.08	2.55 ± 0.08
MINOS+	2.42 ± 0.09	2.48 ± 0.09
NOνA	2.67 ± 0.12	2.71 ± 0.12
Average	2.49 ± 0.04	2.56 ± 0.04

Table 3.1: Values of Δm^2_{32} (NH/IH) based on Daya Bay [13], RENO [30], T2K [11], MINOS+ [12], NOνA [29] experimental results as they were presented at *Neutrino 2016* conference. Corresponding averages are in the bottom row.

3.3.5 Analysis of experimental results

With respect to the fact that the newest results come in the form of Δm^2_{32} (NH/IH), *Method 3* is best suited for data analysis.

It is important to have data from both reactor and accelerator (anti)neutrinos experiments, even when using *Method 3.* Let's look at the difference between $|\Delta m^2_{32}|$ (IH) and Δm^2_{32} (NH) coming from a single experiment as listed in Table 3.1. As we can see there and as it follows from Eq. 3.21, it is fixed on about $0.10 \cdot 10^{-3}$eV^2 for reactor antineutrino experiments. However, when we use

Eqs. (3.19), (3.20) to calculate $P(NH)$ and $P(IH)$ for a pair of experiments with the same difference between $|\Delta m^2_{32}|$ (IH) and Δm^2_{32} (NH), the result is always $P(NH) = P(IH) = 50\%$. Such combination does not provide any information about the hierarchy.

The situation is a bit more complicated for accelerator neutrino experiments. Since $\Delta m^2_{\mu\mu}$ is closer to Δm^2_{32} than Δm^2_{ee}, the difference between $|\Delta m^2_{32}|$ (IH) and Δm^2_{32} (NH) is smaller than in the case of reactor antineutrino experiments. It is not the same for all accelerator neutrino experiments (T2K, NOνA: $0.04 \cdot 10^{-3}\text{eV}^2$, MINOS+: $0.06 \cdot 10^{-3}\text{eV}^2$), but the spread is smaller than for a combination of reactor antineutrino & accelerator neutrino experiments.

For this reason, only combinations of reactor antineutrino & accelerator neutrino experimental results were used for analysis of pairs. For the analysis of all results together, it is similarly important to use results from both types of experiments.

When all results are analysed together in the way described above, the overall preference is for IH with $P(NH) = 42\%$, $P(IH) = 58\%$. Similarly, we can calculate $P(NH)$ and $P(IH)$ for pairs of experiments. The results are in Table 3.2.

Experiments	$P(NH)$	$P(IH)$
Daya Bay & T2K	47%	53%
Daya Bay & MINOS+	53%	47%
Daya Bay & NOνA	37%	63%
RENO & T2K	52%	48%
RENO & MINOS+	52%	48%
RENO & NOνA	49%	51%
All	42%	58%

Table 3.2: Probabilities of NH and IH calculated with *Method 3*.

As we can see, probabilities that depend on RENO results are all close to 50% due to higher uncertainties in RENO experiment. More precise Daya Bay results in combination with similarly precise results of accelerator neutrino experiments provide more significant probabilities, but still far from resolving power for neutrino mass hierarchy.

Now we shall investigate how the situation would change if the precision of measurements increased. For that purpose, we shall use the analysis of pairs. We shall take the same mean values of Δm^2_{32} (NH/IH) as they were measured and then we shall vary the uncertainties to see corresponding probabilities. Results are shown in Fig. 3.4.

As we can see, $P(MH)$ exceeds 90% around $\sigma = \sigma_e = \sigma_\mu = 0.02 \cdot 10^{-3}\text{eV}^2$ for Daya Bay & T2K and Daya Bay & MINOS+ combinations of mean values. For Daya Bay & NOνA combination, $P(IH)$ exceeds 90% around $\sigma = 0.05 \cdot 10^{-3}\text{eV}^2$, but in such case results from one experiment would be more than 3σ away from results of the other one for both Δm^2_{32} (NH) and Δm^2_{32} (IH).

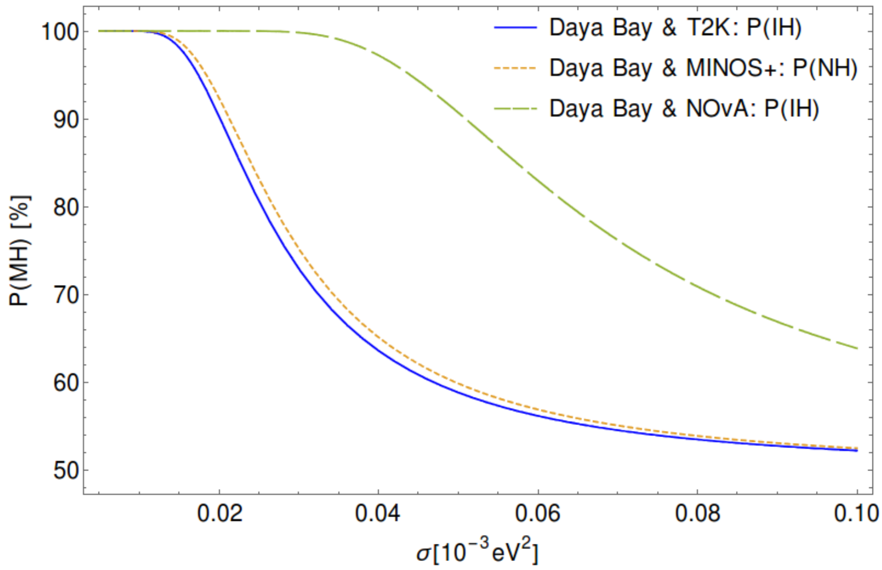

Figure 3.4: *Method 3:* Probability of NH or IH if standard deviations of Δm^2_{32} measurements performed by mentioned experiments were σ, but mean values remained the same. The blue line represents $P(IH)$ based on Daya Bay & T2K mean values of Δm^2_{32} (NH) and Δm^2_{32} (IH). Dashed orange line represents $P(NH)$ based on Daya Bay & MINOS+ combination and dashed green $P(IH)$ based on Daya Bay & NOνA combination.

It is also worth noting that precisions planned in future experiments JUNO and DUNE/LBNF are $0.013 \cdot 10^{-3}\,\text{eV}^2$ and $0.004 \cdot 10^{-3}\,\text{eV}^2$ respectively [27, 31]. Such precisions will mean significant increase in resolving power of this method for neutrino mass hierarchy determination.

4. Measurement of RPC properties for JUNO experiment

Resistive plate chamber (RPC) is a gaseous detector for ionizing radiation. As many other detector types, it takes advantage of charge multiplication in high electric field in gas. There are several types of RPCs differing in various aspects, but they all share certain properties. They are fast detectors with good time resolution (down to 50 ps [32]) and they can be cheaply manufactured in great numbers. RPCs were considered as an option for cosmic muon tracker in JUNO experiment, but as OPERA detector is to be dismounted, its target tracker made of scintillating strips will be used instead [27].

4.1 Design and properties of RPC

Even though many aspects may differ, all RPCs share certain common features. They consist of a gas chamber enclosed by two planar electrodes made from a material with high volume resistivity, typically Bakelite ($\sim 10^{10} - 10^{12}\,\Omega$cm [32, 33]) or glass ($\sim 10^{12}\,\Omega$cm[32]). From the outer side, there is coating made from conductive material, e.g. graphite. High voltage is attached to it so together with insulator plate it works as an electrode with characteristic properties. To obtain signal from RPC, there are readout strips separated from electrodes by insulator.

Ionizing particle passing through the gas gap has a chance of creating clusters of free charge carriers (electrons and ions) along its way. They are accelerated by the electric field. Electrons driven to anode can hit molecules of gas and create more electron-ion pairs. As the number of electrons (and ions) multiplies, an avalanche develops.

For RPCs operated in avalanche mode, further development of the avalanche into a streamer is an unwanted side effect. The signal is induced in readout strips by movement of charge in the avalanche.

If the RPC is operated in streamer mode, further development of the avalanche

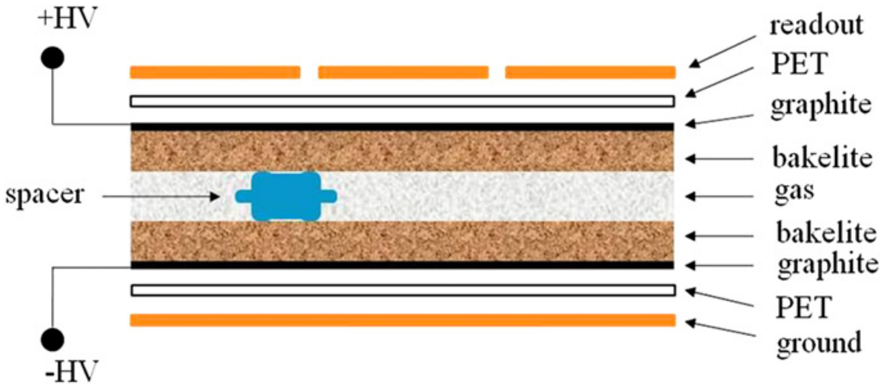

Figure 4.1: Schemes of Daya Bay RPCs and the ones we used for measurement. For other RPCs, materials may vary but the design generally remains similar. This figure is taken from [33].

into a streamer is desirable. It happens when photons start contributing to the avalanche propagation [32]; a chain of avalanches appears and merges into a streamer and possibly creates a conductive link between electrodes. However, the discharge is limited to only a small area around the conductive link due to the high volume resistivity of the electrodes. It creates a blind spot for a certain period of time, but rest of the detector can keep on working unaffected. The advantage of streamer mode is that the signal induced in readout strips is strong and can be directly discriminated without pre-amplification.

RPCs have found use in various experiments (usually when large area needs to be covered thanks to its low price), such as BELLE, OPERA, Daya Bay or ATLAS and ALICE in CERN.

4.2 Measurement of RPC performance

We measured properties of one, later two RPCs operated in streamer mode. They were made by IHEP in China, their design based on the design of RPCs used in the Daya Bay experiment. However, our RPCs are significantly smaller; they are 50×25 cm in size while those used in Daya Bay are 210×110 cm or 210×100 cm. Nonetheless, they both have 2 mm wide gap enclosed by 2 mm thick Bakelite plates coated with graphite on the outside and another $100\,\mu m$ layer of PET. We also used a PE foils to separate readout strips and ground plane made from sheets of copper-clad FR-4 [33].

The measurement took place in several phases:

- During **phase I**, some of first RPC's (from now on, it will be denoted RPC1) properties were measured when it was exposed to cosmic muons. Meanwhile, work was done to measure more and control the whole process by computer.
- During **Training** phase, second RPC (from now on, it will be denoted RPC2) was "trained". The training is a procedure aimed to secure good detector performance afterwards. Note that RPC1 did not endure any training.
- During **phase II** both RPCs were deployed and their properties were measured, again by exposition to cosmic muons. Unfortunately, it was terminated by failure of the gas system.

Even though it was not the first phase chronologically, it is logical to look at the *training* of RPC2 first.

4.2.1 Training of RPC2

The training is a procedure aimed to enhance detector performance afterwards. During this procedure, the electrodes were under high voltage (10 000 V in our case, one electrode being at +5 000 V and the other one −5 000 V) while pure Argon (Ar) was flowing through the chamber. This procedure should lead to "burning" of protrusions on surfaces of the resistive plates, thus reducing their unevenness.

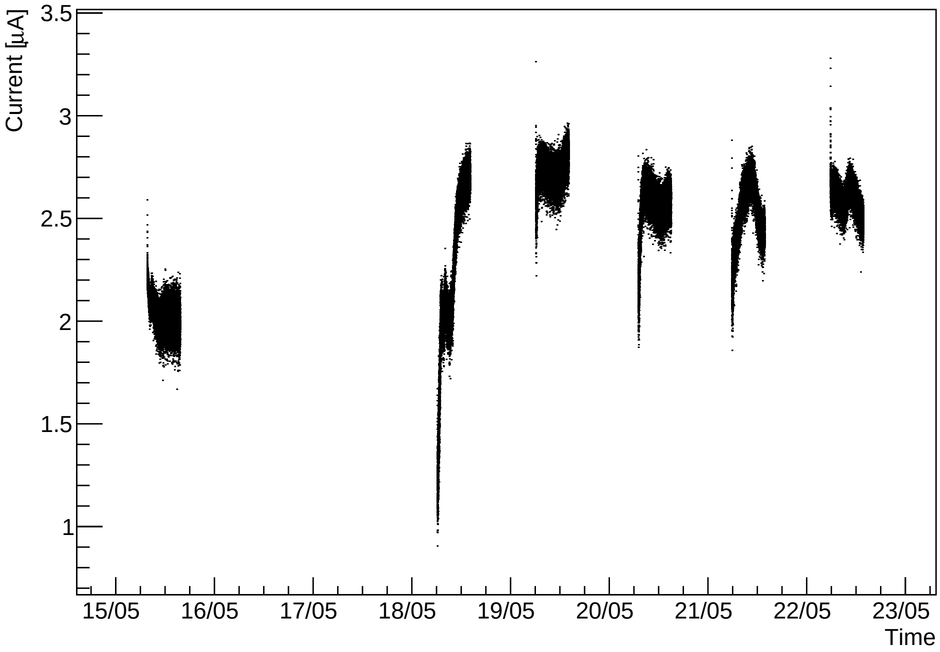

Figure 4.2: Training current on each of training days. Note that during 18/5 mean value of training current shifted from about 2.0μA to about 2.7μA probably due to the increase of the room temperature.

The training was taking place during 6 days; each day for 8 h which makes 48 h in total (in [33] at least 48 h is recommended). During first 5 days, gas flow was activated only along with the high voltage, but between 5^{th} and 6^{th} day the gas flow kept on going. The flow was $2\,\text{cm}^3/\text{min}$ (in [33] they used $100\,\text{cm}^3/\text{min}$ which is about $5\,\text{cm}^3/\text{min}$ when recalculated to the size of our RPC). When there was voltage on RPC2, current through it was measured. Results are shown in Fig. 4.2.

Several thing in Fig. 4.2 are worth noting. There is a change of level of current on 18/5 which coincides with increase of temperature of the room where the measurement was conducted from 22°C to 25°C. Another remarkable thing is that save for the last day there was a $1 - e^{-t}$ type of relaxation with relaxation time of about $\tau_1 \sim 30\,\text{min}$ [1]. It can be better seen in detail from 20/5 in Fig. 4.3. The nature of its occurrence points to the possibility that if there is no flow of gas through RPC for hours or longer, it takes time $\sim \tau_1$ for the gas and conditions in RPC chamber in general to stabilize.

The last thing worth noting is that there is also e^{-t} type of relaxation with relaxation time $\tau_1 \sim 15-30\,\text{s}$. One could think that charging of RPC is responsible, but according to [32] that should be $\lesssim 1\,\text{s}$ for Bakelite specified in [33].

---

[1] Such relaxation is also lacking on the first day of training. By then, the procedure of training was being worked on and it is possible that gas started flowing before beginning of the measurement.

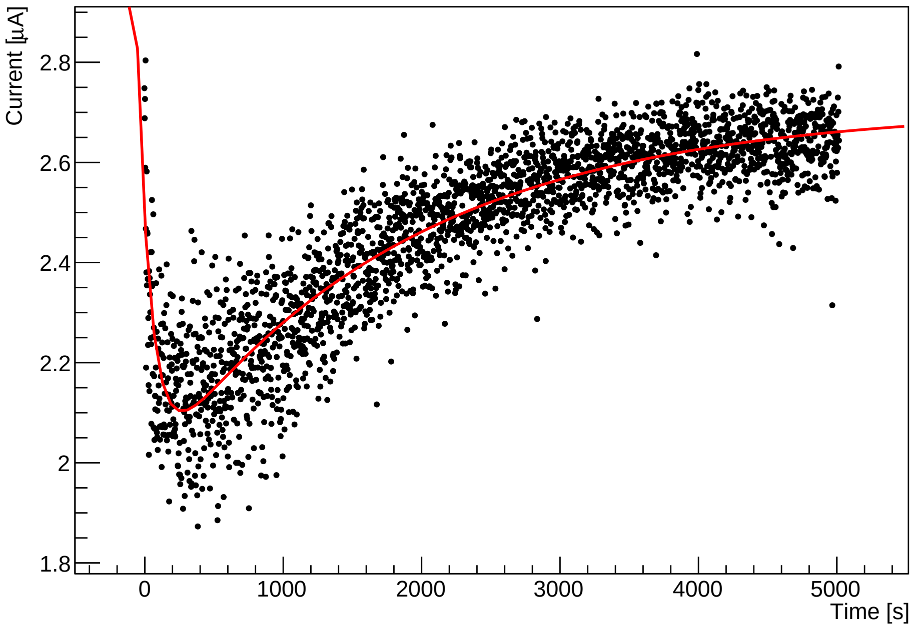

Figure 4.3: Training current on 20/5 with outlining of the relaxation processes.

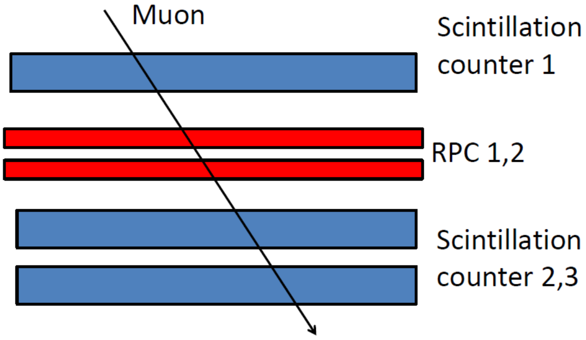

Figure 4.4: Experiomental scheme. The RPCs are "sandwiched" by scintillation counters.

4.2.2 Detector properties of RPCs

Detection efficiency and other properties of RPC1 and later RPC2 were measured during phases I and II. The experimental scheme is shown in Fig. 4.4. In phase I only RPC1 was present, in phase II both RPCs were on the same gas pipe. To recognize the events of interest – cosmic muons passing through RPCs, three scintillation counters were used as a telescope, one above RPCs and two bellow.

Using this experimental layout, the measurement was conducted in cycles. Every cycle, the voltage on RPCs was varied from 6000 V to 8000 V in phase I and from 5800 V to 7800 V in phase II with the step of 100 V. Each point was measured for 325 s and then another one in an increasing manner[2]. Usually, 4 cycles were conducted per day.

---

[2] The duration of 325 s was chosen so that number of singles during this period does not exceed the limit of the scaler we used which is 65535.

During the measurement, specific gas mixture (tested in Daya Bay) was flowing through RPCs:

- 65% Argon
- 31% R-134a freon (1,1,1,2-Tetrafluoroethane)
- 4% Isobutane

In phase I, the gas flow was 2 cm^3/min so that the gas in the volume of RPC changed every 2 hours. In phase II, when both RPCs were on the same gas pipe, the flow was doubled.

In this experimental set-up, following quantities were measured:

- Signals from single scintillation counters t_1, t_2, t_3.
- Coincidence of all 3 scintillation counters c_s.
- Voltage on RPCs $V = V_1 = V_2$.
- Signals from single strips of RPCs.
- Signals from whole RPCs (*or* signal from both strips for each RPC) r_1, r_2.
- Coincidence of either RPC and all 3 scintillation counters c_1, c_2.
- Current in RPCs I_1, I_2.

RPC signals were discriminated at 200 mV level (whereas in [33] it was 50 mV). This level was chosen with respect to the fact that background significantly increased below this level.

Unfortunately, during data analysis it appeared that there had been certain problems with the readout of the second strip of RPC2. At random points in time, it was producing permanent signal lasting up to several 325 s periods. The periods during which this happened were identified and not used for further data analysis.

Apart from that, failure of high-voltage supply occurred few times.

RPC efficiency

Determining the dependence of RPC efficiency on voltage was our main interest. For this purpose, the efficiency of RPCi e_i ($i \in \{1, 2\}$) is defined as number of coincidences of RPCi and all 3 scintillation counters over coincidences of all 3 scintillation counters:

$$e_i \equiv \frac{c_i}{c_s} \quad i \in \{1, 2\} \tag{4.1}$$

It is based on the assumption that coincidences of all 3 scintillation counters are almost solely caused by muons from cosmic rays and such muons have to pass through RPCs as well. Thus we can look whether such muons create signals (over threshold) in RPCs or not. The mean frequency of coincidences of all 3 scintillation counters was 1.15 s^{-1}.

Both the dependence of efficiency on voltage and its evolution from cycle to cycle were investigated. In a single cycle, a combination of error function

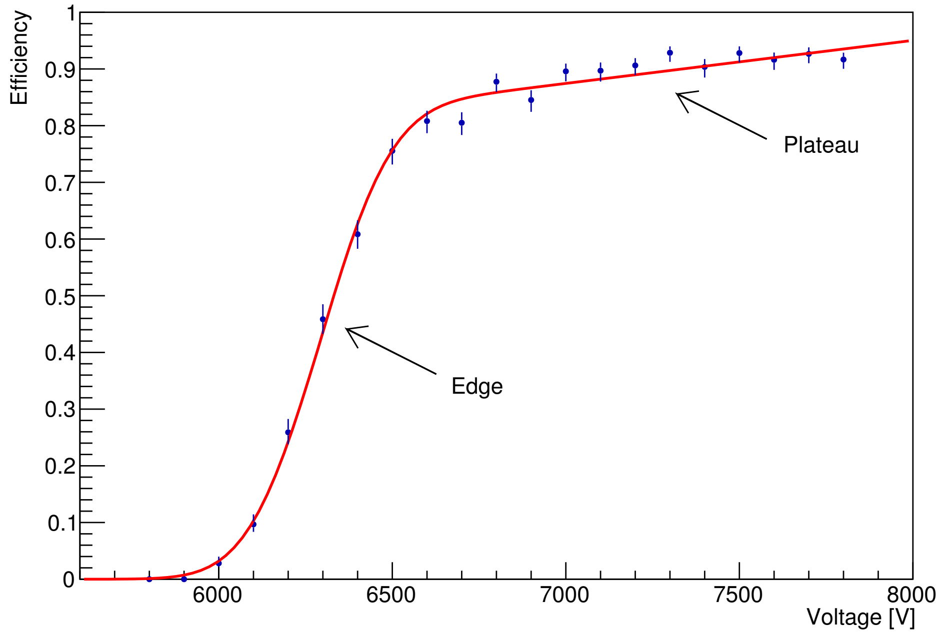

Figure 4.5: Dependence of efficiency on voltage in the 3$^{\text{rd}}$ cycle on 10.6. fitted with combination of error function and linear function.

and linear function was used to approximate the curve. An example of one cycle from 10/6 is shown in Fig. 4.5. One can see that the efficiency steeply grows from approximately 6000 V to 6500 V. The growth is characterized by error function and this area of steep growth will be denoted “edge”. It appeared that the efficiency keeps growing even after that (albeit slowly) within the range of measurement. Although it is obvious that the growth cannot keep continue ad infinitum, it was approximated by linear function in measured range in order to reduce the number of free parameters. This area of slow increase will be denoted “plateau”.

Before we discuss what efficiencies were reached in the plateau area, let’s first investigate the development of RPC performance over the course of time (days). The situation was significantly different for RPC1 and RPC2. While RPC2 was trained as described above, RPC1 was not. On the other hand, measurement of its performance was conducted in phase I. It appeared that in the beginning of phase I RPC1 reached lower efficiency close to the end-point (8000 V) than at the end of phase I while the growth was slower and started at higher voltage. The difference can be seen in Fig. 4.6. In Fig. 4.6(a) RPC1 reaches efficiency of only $\sim$ 70% compared to $\sim$ 90% in Fig. 4.6(b). Moreover, the growth of efficiency starts in Fig. 4.6(a) at voltage higher by $\sim$ 300 V than in Fig. 4.6(b) and is slower. It is apparent that the performance of RPC1 increased significantly during phase I.

On the other hand, if we compare performances of RPC1 and RPC2 in the beginning of phase II (when RPC1 had endured about 200 h of measurement and RPC2 about 50 h of training) in Fig. 4.7, we see that their efficiency curves are very similar. We can conclude that the training of RPC2 and measurement of RPC1 in phase I had similar effect on their performance. That is not surprising

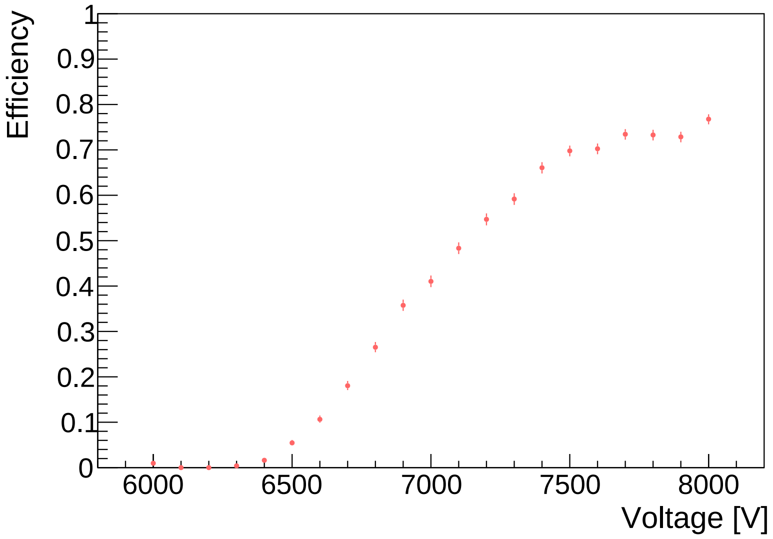

(a) Beginning of phase I (7/4)

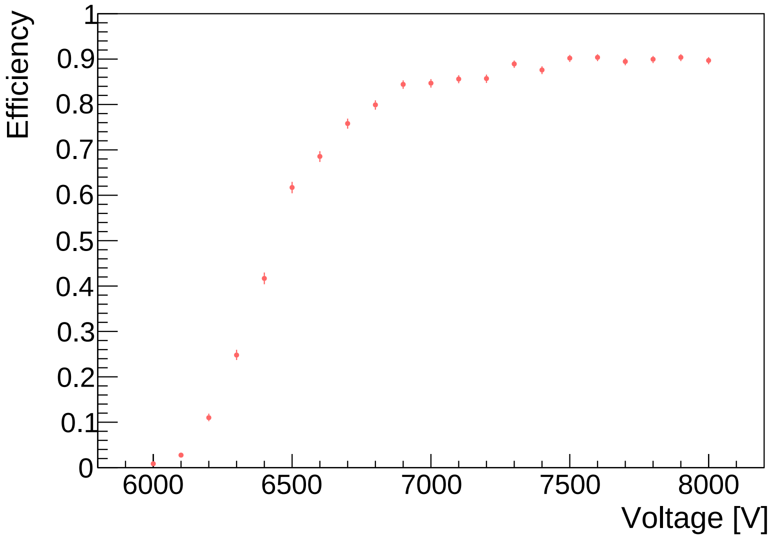

(b) End of phase I (13/5)

Figure 4.6: Comparison of dependence of RPC1 efficiency on voltage in beginning of phase I and at the end.

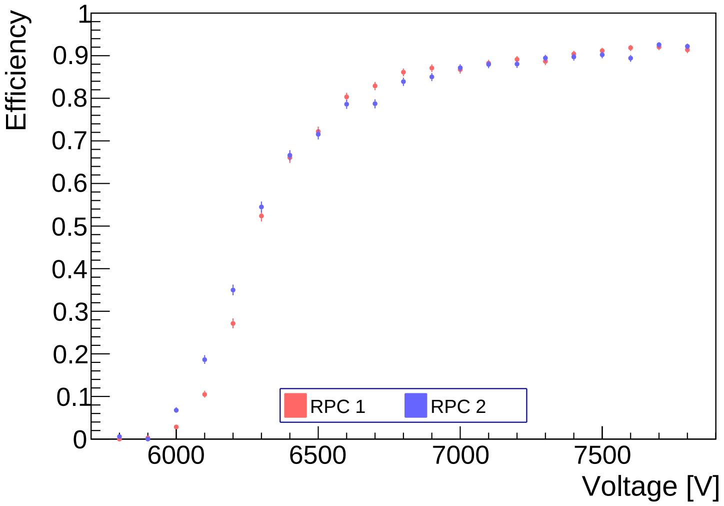

Figure 4.7: Dependence of RPCs' efficiencies on voltage in the beginning of phase II (3/6). Both RPCs show similar performance.

because RPC1 was under high voltage during measurement in phase I making the process in principle similar to training.

Now let's look at the efficiencies that were reached during phase II. In the plateau area close to the end-point (7800 V), the efficiency was consistently over 90% for RPC1 and 89% for RPC2. The average efficiency in 7500 V - 7800 V region thorough the cycles of phase II is shown in Fig. 4.8. Horizontal lines denote the overall average efficiency. It is 91.7% for RPC1 and 91.2% for RPC2.

Looking at Fig. 4.8 it seems that there is still slight increase of RPCs' performance in terms of end-point efficiencies over the course of phase II.

According to [33] efficiency over 94% at 8000 V was required for Daya Bay RPCs during quality control, but in different conditions. They had RPCs of different size with 50 mV threshold for discrimination and a different gas ratio in mixture – argon : R-134a : isobutane = 53 : 43 : 4.

When the efficiencies were measured in Daya Bay experimental halls with gas mixture – argon : R-134a : isobutane : SF_6 = 65.5 : 30.0 : 4.0 : 0.5 and threshold 35 mV, on average they were greater than 90% in two halls and lower than 90% in one hall [34].

Another area of interest concerning efficiency is the position of the edge. For the following analysis the position of the edge was considered to be the midpoint (inflection point) of the error function with which the efficiency dependence on voltage was fitted.

During phase I the edge of RPC1 moved from about 6700 V down to about 6400 V along with the increase of end-point efficiency described above. Edge positions during phase II are shown in Fig. 4.9. Most of the values lie within 6150 V - 6350 V region. RPC2 perform consistently better than RPC1 (in the sense that the edge is on lower voltage), however the day-to-day variations are of similar size as the difference between RPC1 and RPC2.

There is however one point in Fig. 4.9 that stands out - the position of RPC2 edge at about 6600 V in the first of 8/6 cycles. If we look closely, we see that the

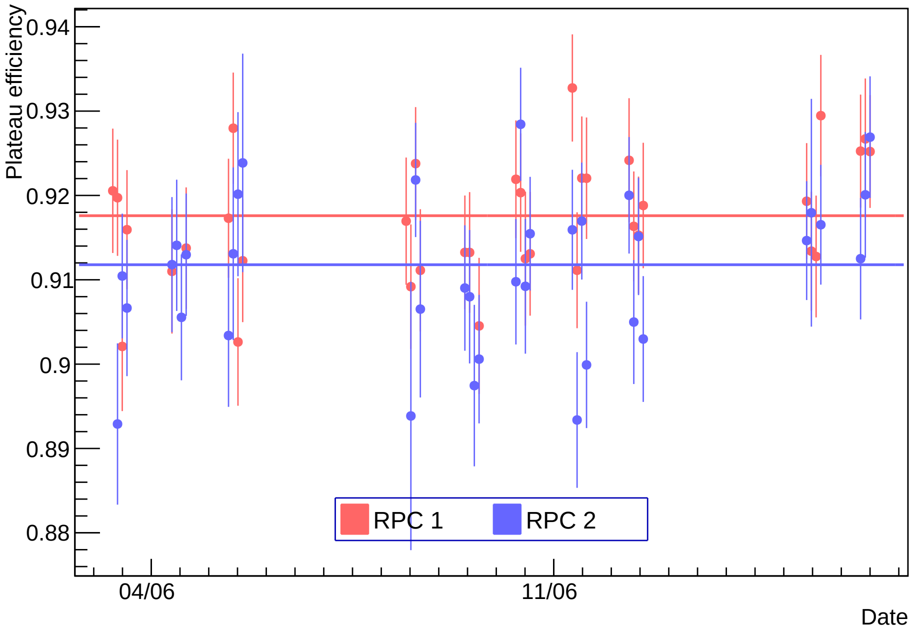

Figure 4.8: Average efficiency in 7500 V - 7800 V region cycle by cycle during phase II. Horizontal lines denote the overall average efficiency.

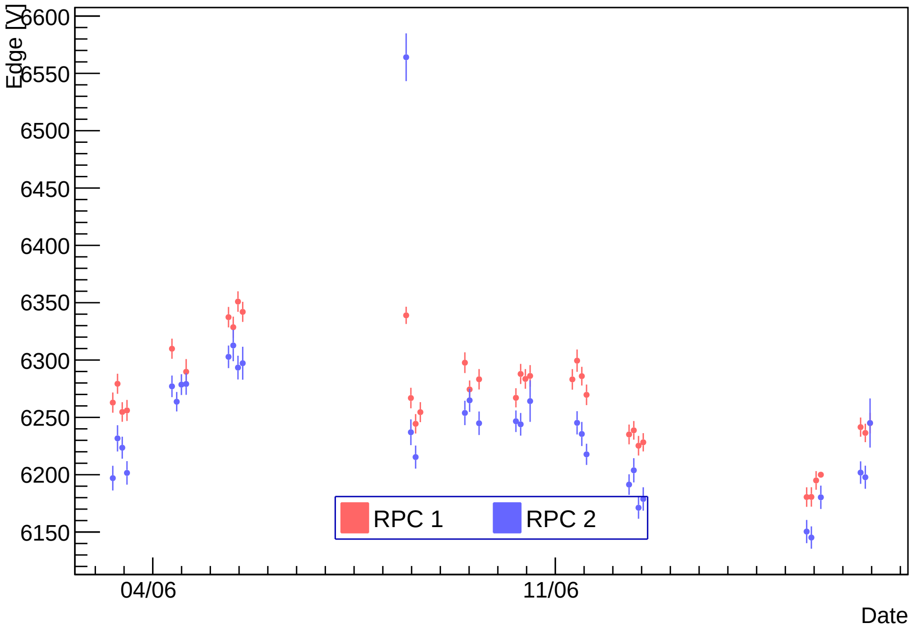

Figure 4.9: Position of the edge defined as the midpoint (inflection point) of the error function with which the efficiency dependence on voltage was fitted.

analogous point for RPC1 is also significantly higher than the rest from the same day. Similar phenomenon occurred during phase I as well. Four times (out of six weeks) the position of edge was around 200 V higher in the first cycle after weekend. Unfortunately, gas flow was controlled manually in not an exact manner. It was usually turned on 10 − 30 minutes before beginning of the measurement. Nevertheless, one can still conclude that if RPC is not used for few days, its performance is temporarily deteriorated, but gets back to previous level within 2 h (1 cycle) of RPC usage (gas flow and high voltage).

With respect to results from training it seems more probable that this phenomenon is caused primarily by long (in order of days) absence of gas flow. If it were solely due to the absence of high voltage, it should have happened every time high voltage is off. That includes 15/6 when it did not happen and when the gas flow was actually activated during preceding weekend. It is likely that fresh gas and continuous flow are necessary for good performance of RPC.

It was suggested in [34] that humidity may have the effect described above (shift of the curve to higher voltages and lower efficiency).

RPC singles and current

Only a small fraction of signals produced by RPCs are actually linked to coincidence of scintillation counters and used to determine RPCs' efficiency. While these coincidences are produced with frequency of about $1\,\mathrm{s}^{-1}$, RPCs produce over 100 signals/s close to the end-point of measurement. These signals, denoted "singles", are part of RPC performance and were investigated.

It appeared that starting at a certain voltage there is approximately a linear growth in the frequency of singles; for RPC1 it tends to be slightly concave, for RPC2 slightly convex. An example from the last day of phase II (16/6) of both RPCs is shown in Fig. 4.10 along with a linear fit. The inclination was generally bigger for RPC2 by even as much as 50%.

The quality control [33] required the singles frequency per cm^2 to be lower than $0.80\,\mathrm{s}^{-1}\mathrm{cm}^{-2}$ at 8000 V in conditions described above. The average value they obtained was $0.15\,\mathrm{s}^{-1}\mathrm{cm}^{-2}$. Our measurement ended at 7800 V but extrapolating data linearly we would expect both RPCs to be in $0.10 - 0.20\,\mathrm{s}^{-1}\mathrm{cm}^{-2}$ interval at 8000 V.

It is interesting to compare the inclination of the dependence of singles frequency on voltage of RPC1 in phase I and phase II. As it can be seen in Fig. 4.11, the frequency of singles was declining thorough phase I. Next follows the gap during which training of RPC2 and preparation of phase II set-up took place and the room temperature increased. With beginning of phase II, the level of inclination is notably higher. Then again another decrease is hinted, albeit slower if any at all.

We have seen above the effect that temperature increase had on training current. It is likely that the higher temperature causes higher inclination of singles frequency, because (as we shall see now) singles and currents in RPCs are naturally connected. Nonetheless, another measurement especially aimed to investigate the temperature influence on RPC performance would be certainly useful to deepen our understanding.

The dependence of current on singles frequency for RPC1 and RPC2 is shown in Fig. 4.12. However, there is certain inaccuracy caused by the fact that while

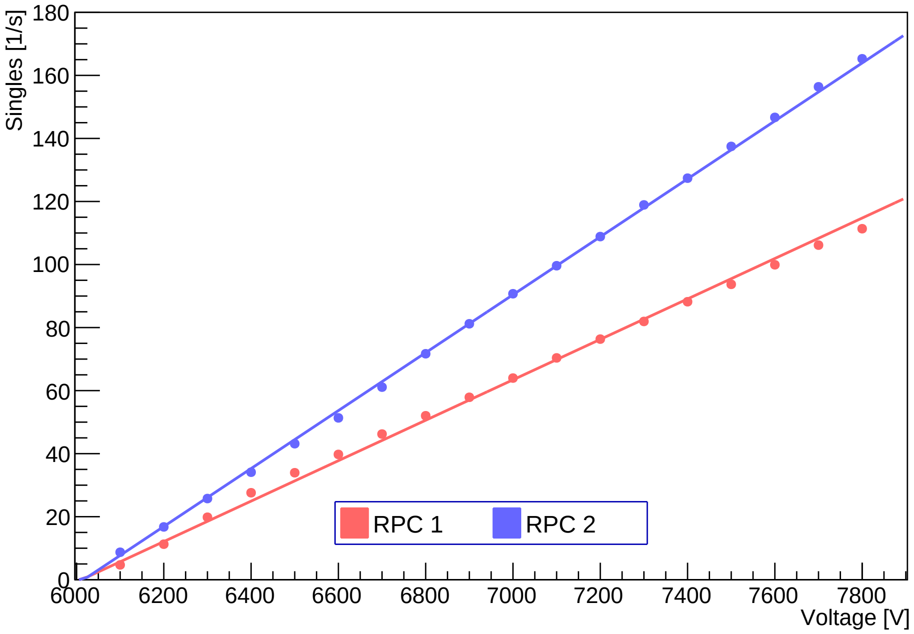

Figure 4.10: Dependence of frequency of singles on voltage (measured in second cycle on 16/6) along with a linear fit. RPC1 is denoted by red colour, RPC2 by blue.

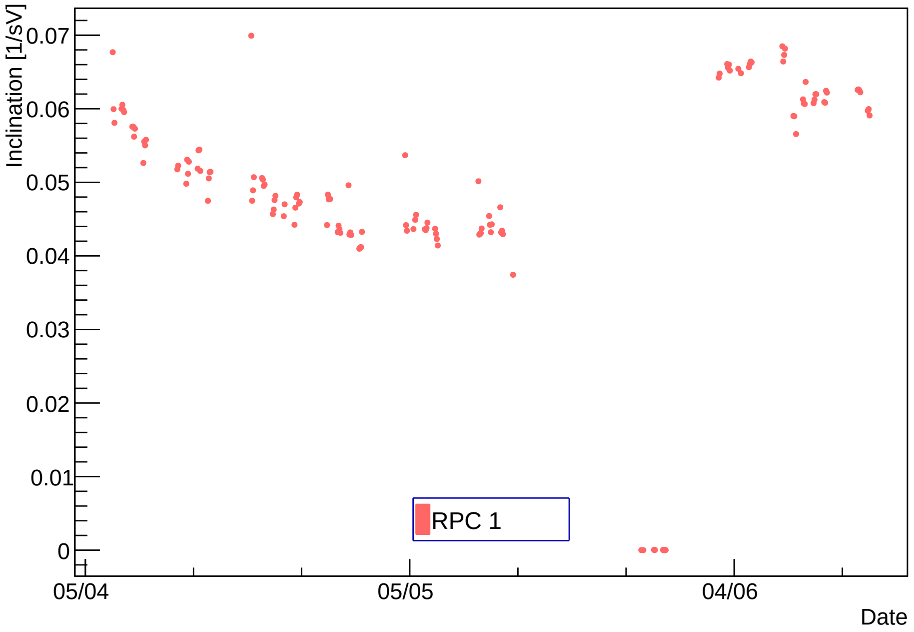

Figure 4.11: Inclination of singles frequency dependence on voltage for RPC1 thorough phase I and phase II. The zero values correspond to preparation of phase II set-up.

singles frequency is measured from the total number of singles in the particular period and duration of the period, the current was measured at one point at the end of the period.

We can see in Fig. 4.12 that the current increases with singles frequency as expected, however the nature of this increase if slightly different for RPC1 and RPC2. The increase is almost linear in case of RPC2 and overall the current and the frequency of singles are bigger at a given voltage than those of RPC1. On the other hand, in case of RPC1 the growth seems to be of higher power than linear. When fitted with $p_0 + p_1 x^{p_2}$ function, the best-fit power p_2 was about 1.5 for RPC1 and 1.1 for RPC2 (close to linear as expected).

It should be noted that while the value of current is given, the number of singles and their frequency depend on the discrimination level used, i.e. how big the signal must be to be counted. It would certainly be interesting to change the discrimination level to see if the difference between the curves in Fig. 4.12 can be reconciled that way or not.

Another property that can be determined is the starting point of singles, i.e. the voltage at which singles frequency starts to grow linearly. It is shown in Fig. 4.13. It follows the same pattern as the position of edge in Fig. 4.9, but in contrast to that the growth of singles starts at the same voltage for both RPCs. The characteristically high value of edge position of RPC2 in the first cycle on 8/6 is not reflected in Fig. 4.13, because in that cycle, the growth of singles frequency is not linear and linear fit does not yield good result.

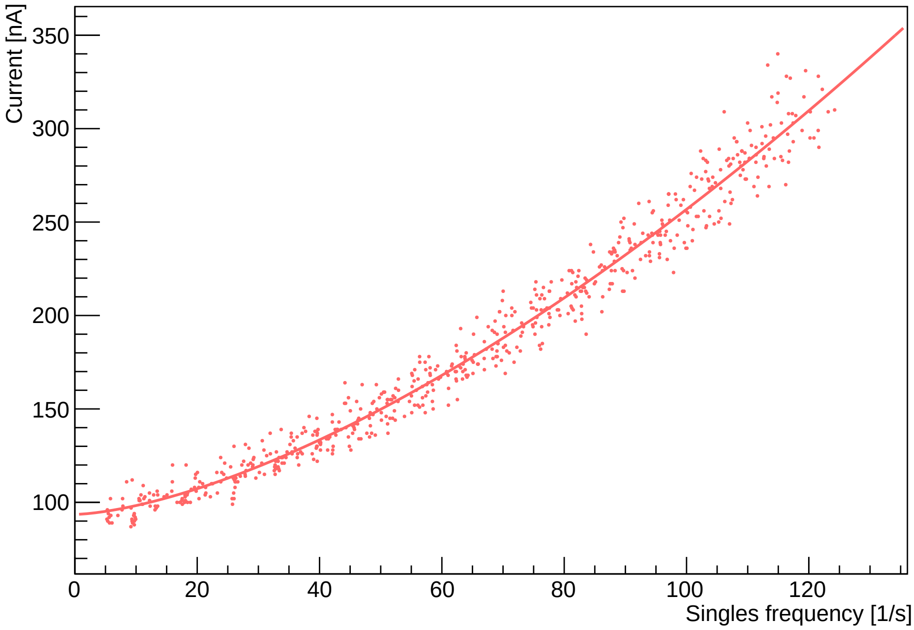

(a) Current-singles frequency dependence of RPC1

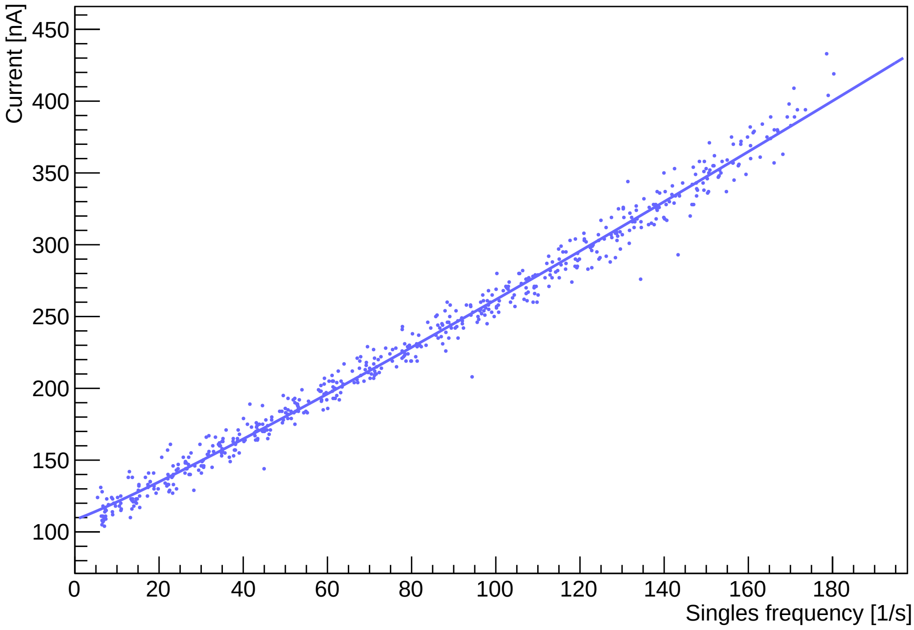

(b) Current-singles frequency dependence of RPC2

Figure 4.12: Current-singles frequency dependence of RPC1 and RPC2. They were both fitted by $p_0 + p_1 x^{p_2}$ function. While the growth of RPC2 current is nearly linear (with best-fit value $p_2 \doteq 1.1$), the growth of RPC1 is steeper (with best-fit value $p_2 \doteq 1.5$).

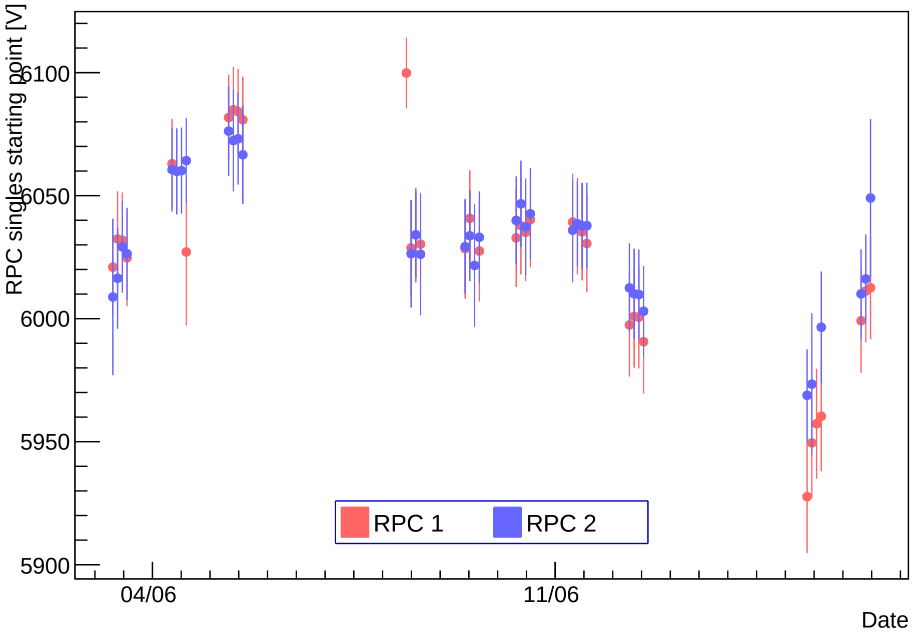

Figure 4.13: Voltage at which singles frequency starts to grow linearly. Each point corresponds to one cycle.

Conclusion

In the beginning of this thesis, the possibilities of Dirac and Majorana origin of neutrino masses were described. It is still not known whether neutrinos are their own antiparticles or not. Experiments measuring neutrinoless double beta decay address this question. As we saw, knowledge of neutrino mass hierarchy is important for interpretation of their results.

After section dedicated to neutrino mass origin, the status of direct search for neutrino masses was presented. Following that, neutrino mixing was introduced, first in general and then we embraced the three active neutrino framework which we used in the rest of this thesis. PMNS matrix and its parametrization were described. Using that, the phenomenon of neutrino oscillation was elaborated in more detail. That includes oscillations in vacuum and matter as well, because matter effect on neutrino oscillations is important for determining neutrino mass ordering. Finally, current values of oscillation parameters were shown with a brief explanation how they were obtained.

In the second part of this thesis, the focus was on the neutrino mass hierarchy. After explanation of the difference between so called *normal* and *inverted* hierarchies, reasons for neutrino mass hierarchy determination followed. Neutrinoless beta decay (which had been already mentioned in relation with question of Dirac vs. Majorana nature of neutrino) and measurement of CP-violating phase δ were presented in more detail. After that, possible approaches to the mass hierarchy problem were listed. More attention was given to JUNO which is currently under construction. RPCs were originally considered as an option for its muon tracker and measurement of RPC properties is also part of this thesis. However, as the OPERA detector is to be dismounted, its target tracker made of scintillating strips will be used instead.

After overview of possible approaches to the mass hierarchy problem, a part dedicated to one of them ensued. This approach is based on comparison of mass splitting measured in disappearance experiments with reactor $\overline{\nu}_e$ and accelerator ν_μ. Several methods were explored. Two of them use the effective mass splitting Δm^2_{ee} and $\Delta m^2_{\mu\mu}$. The third one compares Δm^2_{32} obtained from $\overline{\nu}_e$ and ν_μ disappearance measurements. Analysis of the experimental data ensued. It resulted in overall preference of 58% for inverted hierarchy. More significant results can be expected with precisions planned in future experiments.

In last part, RPC design and principle of operation were explained first and then results from measurement of properties of two Daya Bay type RPCs followed. It appeared that 50 h of training enhanced RPC detection capability in a similar way as 200 h of use. Efficiencies for cosmic muons detection were measured to be over 91%. Apart from that, singles and currents were measured and analysed as well.

Bibliography

[1] S. Bilenky. *Introduction to the Physics of Massive and Mixed Neutrinos.* Springer, Berlin Heidelberg, 2010.

[2] K. Zuber. *Neutrino Physics.* Second edition. Taylor and Francis Group, Boca Raton, 2012.

[3] V.N. Aseev et al. An upper limit on electron antineutrino mass from Troitsk experiment. *e-Print arXiv:1108.5034v3 [hep-ex]*, 2011.

[4] Ch. Kraus et al. Final results from phase II of the Mainz neutrino mass search in tritium beta decay. *e-Print arXiv:hep-ex/0412056v2*, 2005.

[5] D.S. Parno. The Katrin experiment: Status and outlook. *e-Print arXiv:1307.5289v1 [physics.ins-det]*, 2013.

[6] A. Gando et al. (KamLAND-Zen Collaboration). Search for majorana neutrinos near the inverted mass hierarchy region with KamLAND-Zen. *e-Print arXiv:1605.02889v1 [hep-ex]*, 2016.

[7] B. Kayser. Neutrino oscillation phenomenology. *e-Print arXiv: 0804.1121v3 [hep-ph]*, 2008.

[8] T. Davídek and R. Leitner. *Elementární částice od prvních objevů po současné experimenty.* První vydání. Matfyzpress, Praha, 2012.

[9] B. Aharmim et al. (SNO Collaboration). Combined analysis of all three phases of solar neutrino data from the Sudbury Neutrino Observatory. *e-Print arXiv:1109.0763v1 [nucl-ex]*, 2011.

[10] K.A. Olive et al. (Particle Data Group). *Chin. Phys. C*, page 38, 2014 and 2015 update.

[11] H. A. Tanaka (T2K collaboration). Recent results from the Daya Bay experiment. *Neutrino 2016 Conference presentation.*

[12] J. Evans (MINOS, MINOS+ collaboration). New results from MINOS and MINOS+. *Neutrino 2016 Conference presentation.*

[13] Y. Zeyuan (Daya Bay collaboration). T2K: Latest results. *Neutrino 2016 Conference presentation.*

[14] F. Capozzi et al. Neutrino masses and mixings: Status of known and unknown 3nu parameters. *e-Print arXiv:1601.07777v1 [hep-ph]*, 2016.

[15] H. Nunokawa et al. CP Violation and neutrino oscillations. *e-Print arXiv:0710.0554v2 [hep-ph]*, 2007.

[16] E. Andreotti et al. (CUORICINO Collaboration). 130te neutrinoless double-beta decay with CUORICINO. *e-Print arXiv:1012.3266v1 [nucl-ex]*, 2010.

[17] J. B. Albert et al. (EXO-200 Collaboration). Search for 2vbb decay of 136xe to the 0+1 excited state of 136ba with exo-200. *e-Print arXiv:1511.04770v1 [nucl-ex]*, 2015.

[18] G. Benato et al. (GERDA Collaboration). Search of neutrinoless double beta decay with the GERDA experiment. *e-Print arXiv:1509.07792v1 [nucl-ex]*, 2015.

[19] R. Arnold et al. (NEMO-3 Collaboration). Measurement of the double-beta decay half-life and search for the neutrinoless double-beta decay of 48Ca with the NEMO-3 detector. *e-Print arXiv:1604.01710v2 [hep-ex]*, 2016.

[20] J. Bernabeu et al. A combined beta-beam and electron capture neutrino experiment. *e-Print arXiv:0902.4903v1 [hep-ph]*, 2009.

[21] F.J.P. Soler. nuSTORM: Neutrinos from stored muons. *e-Print arXiv:1507.08836 [physics.ins-det]*, 2015.

[22] T. Nakaya and R. K. Plunkett. Neutrino oscillations with the MINOS, MINOS+, T2K, and NOvA experiments. *e-Print arXiv:1507.08134v4 [hep-ex]*, 2015.

[23] X. Qian and P. Vogel. Neutrino mass hierarchy. *e-Print arXiv:1505.01891v3 [hep-ex]*, 2015.

[24] J. Bian. The NOvA experiment: overview and status. *e-Print arXiv:1309.7898v1 [physics.ins-det]*, 2013.

[25] S. Moriyama (Super-Kamiokande Collaboration). New atmospheric and solar results from Super-Kamiokande. *Neutrino 2016 Conference presentation.*

[26] F. An et al. (JUNO Collaboration). Neutrino physics with JUNO. *e-Print arXiv:1507.05613v2 [physics.ins-det]*, 2015.

[27] T. Adam et al. (JUNO Collaboration). JUNO conceptual design report. *e-Print arXiv:1508.07166 [physics.ins-det]*, 2015.

[28] H. Nunokawa, S. Parke, and R. Zukanovich Funchal. Another possible way to determine the neutrino mass hierarchy. *e-Print arXiv:hep-ph/0503283v1*, 2005.

[29] P. Vahle (NOvA collaboration). New results from NOvA. *Neutrino 2016 Conference presentation.*

[30] K. K. Joo (RENO collaboration). New results from RENO and prospects with RENO-50. *Neutrino 2016 Conference presentation.*

[31] R. Acciarri et al. (The DUNE Collaboration). Long-baseline neutrino facility (LBNF) and deep underground neutrino experiment (DUNE). *e-Print arXiv:1512.06148v2 [physics.ins-det]*, 2016.

[32] Ch. Lippmann. *Detector Physics of Resistive Plate Chambers.* Frankfurt am Main, 2003.

[33] L. Ma et al. The mass production and quality control of RPCs for the Daya Bay experiment. *Nuclear Instruments and Methods in Physics Research A*, 659:154–160, 2011.

[34] L. Ma et al. Commissioning of RPC detector systems for the Daya Bay experiment. *Chin. Phys. C (HEP & NP)*, 34(8), 2010.